AWARD NUMBER: W81XWH-22-1-0468

TITLE: Defining and Overcoming a Novel Extracellular Matrix Inhibitor of Remyelination in MS: Fibulin-2

PRINCIPAL INVESTIGATOR: Dr. V. Wee Yong

CONTRACTING ORGANIZATION: The University of Calgary, Calgary, AB, Canada

REPORT DATE: August 2023

TYPE OF REPORT: Annual

PREPARED FOR: U.S. Army Medical Research and Development Command
Fort Detrick, Maryland 21702-5012

REPORT DOCUMENTATION PAGE

Form Approved
OMB No. 0704-0188

1. REPORT DATE	**2. REPORT TYPE**	**3. DATES COVERED**
August 2023	Annual	01Aug2022-31Jul2023

4. TITLE AND SUBTITLE

Defining and Overcoming a Novel Extracellular Matrix Inhibitor of Remyelination in MS: Fibulin-2

5a. CONTRACT NUMBER

5b. GRANT NUMBER
W81XWH-22-1-0468

5c. PROGRAM ELEMENT NUMBER

6. AUTHOR(S)

Dr. V. Wee Yong

E-Mail:vyong@ucalgary.ca

5d. PROJECT NUMBER

5e. TASK NUMBER

5f. WORK UNIT NUMBER

7. PERFORMING ORGANIZATION NAME(S) AND ADDRESS(ES)

The University of Calgary
Department of Clinical Neuroscience
3330 Hospital Drive NW
Calgary, AB T2N 4N1

8. PERFORMING ORGANIZATION REPORT NUMBER
10037199 (Parent project: 10038483)

9. SPONSORING / MONITORING AGENCY NAME(S) AND ADDRESS(ES)

U.S. Army Medical Research and Development Command
Fort Detrick, Maryland 21702-5012

10. SPONSOR/MONITOR'S ACRONYM(S)

11. SPONSOR/MONITOR'S REPORT NUMBER(S)

12. DISTRIBUTION / AVAILABILITY STATEMENT

Approved for Public Release; Distribution Unlimited

13. SUPPLEMENTARY NOTES
N/A

14. ABSTRACT

In Multiple Sclerosis (MS), oligodendrocytes and the myelin that they make and maintain are lost in the brain and spinal cord. There are spontaneous attempts at repair within lesions, and these take the form of the generation of new oligodendrocytes from oligodendrocyte precursor cells (OPCs). The new oligodendrocytes then extend and reform myelin on nerve fibres that have lost their myelin sheaths. This process is called remyelination. There are many advantages to remyelination, including the restoration of conduction of signals along nerve fibres, and the protection by the newly formed myelin of the denuded nerve fibres from further deterioration. Best yet there might be restoration of lost deficits with remyelination as has been demonstrated in experimental animals where, for example, cats with loss of vision regain sight upon remyelination of the optic nerve. Thus, with spontaneous attempts at repair that occur naturally in MS, and the benefits of remyelination, there are active research efforts ongoing world-wide to seek to enhance remyelination in people living with MS. The repair of myelin would benefit all stages of MS, including progressive MS to slow progression of disability, or to elicit some return of function.

Research at promoting remyelination in people with MS have met with the realization that there are many inhibitors to the repair process within MS lesions. In particular, the lesion is very hostile by containing a number of obstacles to repair, including the aberrant expression of proteins that are called extracellular matrix molecules. We have described one such class of extracellular matrix molecules, the chondroitin sulfate proteoglycans (CSPGs), as inhibitory to myelin repair, and we have been seeking approaches to neutralize CSPGs to promote remyelination. During the course of this research, we have asked if there are other equally (or perhaps even more so) relevant extracellular matrix molecules expressed in MS lesions that might also be critical obstacles to the repair process. By mining public databases, we have discovered that an extracellular matrix molecule, Fibulin-2, is highly expressed in lesions of MS as well as its animal models. There are so far no association of Fibulin-2 with MS outcomes at this point in the literature. Thus, we have gone forth and sought data to determine whether Fibulin-2 is an inhibitor to myelin repair process. Our preliminary results indicate that this is indeed the case. In this proposal, we seek to establish the concept that Fibulin-2 is contained within most MS lesions that do not repair, and we seek to understand how Fibulin-2 inhibits the myelin repair process. This approach will help us to develop new drugs to overcome Fibulin-2. Moreover, we will combine overcoming both Fibuln-2 and the CSPGs to determine whether inhibiting both obstacles would provide a better efficacy of myelin repair in lesions of animal models of MS. We are introducing new strategies, particularly drugs that are targeted to lesions within the brain and spinal cord to overcome CSPGs, and we hope to do the same to overcome Fibulin-2.

In general, these experiments are aimed at establishing the critical importance of Fibulin-2 and also CSPGs, in lesions of MS where they impede the repair process. Besides creating fundamental new knowledge, the experiments will also test new therapeutics in experimental animals so that the repair of lesions occurring in MS can be substantially enhanced in the future. The ultimate goal is to provide a milieu within MS lesions that is very conducive for repair, so that meaningful functional recovery in all forms of MS can be ultimately achieved.

15. SUBJECT TERMS
None listed.

16. SECURITY CLASSIFICATION OF:			**17. LIMITATION OF ABSTRACT**	**18. NUMBER OF PAGES**	**19a. NAME OF RESPONSIBLE PERSON** USAMRDC
a. REPORT	**b. ABSTRACT**	**c. THIS PAGE**	Unclassified	81	**19b. TELEPHONE NUMBER** *(include area code)*
Unclassified	Unclassified	Unclassified			

TABLE OF CONTENTS

Introduction – This grant is focused on the changes to the extracellular matrix (ECM) in lesions of MS. Many ECM molecules have been described in lesions of MS and several of these are thought to inhibit the formation of new oligodendrocytes (oligodendrogenesis) and their maturation to myelin forming cells (remyelination). However, whether there are unknown ECM molecules in MS lesions, and which may have critical properties in regulating lesion recovery remain unclear. In our proposal, we seek to establish fibulin-2 as a hitherto undescribed ECM molecule in MS lesions and our aim is to provide data on the expression of Fibulin-2 in lesions of MS and to ascertain its biological properties. To this end, we have made significant progress in Year 1 of this grant which we are happy to report on below.

Keywords: oligodendrogenesis, remyelination, multiple sclerosis, inhibitor, histology

1. **Accomplishments**
   - **What were the major goals of the project?**

In Year 1, the major goals of the project were to inform on the expression of Fibulin-2 in lesions of MS and its animal models. Moreover, we sought to generate mice that were genetically deficient for Fibulin-2 to determine whether these animals would have an altered response relevant to MS such as in the inflammatory model of experimental autoimmune encephalomyelitis (EAE) and the toxin induced model inflicted by Lysolecithin demyelination.

   - **What was accomplished under these goals?**

We have made substantial progress in Year 1 of the proposed activities. First, we evaluated five cases of autopsied MS specimens and found that in normal-appearing brain, there was no detectable Fibulin-2 immunoreactive protein (that is, no signal detected by immunofluorescence microscopy). However, in active lesions, where immune cells were quite uniformly distributed across the lesion, Fibulin-2 immunofluorescence was prominently elevated. Moreover, in chronic active lesions, where immune cells are aggregated at the rim of the lesion and where the centre of the lesion has few remaining immune cells, Fibulin-2 expression was upregulated at both the rim and the lesion core. The latter finding indicates that once generated and deposited into the lesion environment, Fibulin-2 persists even though the immune activity has subsided. Thus, these results in MS tissue affirm the prominent elevation of Fibulin-2 in areas of injury, and where Fibulin-2 expression is persistent.

We also determined that in the EAE and Lysolecithin models of MS, Fibulin-2 was detected only in demyelinated lesions and not in normal appearing spinal cord areas (brain was not assessed). In animal models we focus on the spinal cord where injury is more prominent in models of MS. In spinal cord lesions of these models of MS, we determined that Fibulin-2 expression was persistent in lesions (that is, the deposited Fibulin-2 is not effectively cleared from lesion).

To ascribe functional roles of Fibulin-2 on regenerative events, we resorted to tissue culture studies where oligodendrocytes were plated onto Fibulin-2 substrates. We found that while initial adhesion of cells was not perturbed, subsequently, cells die as they increase their maturation (acquisition of myelin proteins, increase in morphological complexity) in culture. Fibulin-2 is therefore a non-permissive substrate for oligodendrocyte wellbeing. This is consistent with the results in models of MS, and in

MS lesions, where Fibulin-2 elevation is not associated with increased repopulation of oligodendrocytes.

We next perturbed genetically the expression of Fibulin-2 in mice. We purchased frozen embryos from Jackson laboratory of animals that were genetically null for Fibulin-2. We contracted Jackson laboratories to generate offsprings from the frozen embryos and the offsprings were then sent to us where we bred these animals in house. Mating the null mice with wild type animals, and then re-mating the next generation, we obtained mice that were genetically wildtype, heterozygote for Fibulin-2 deletion, or Fibulin-2 homozygote deletion. These animals were then subjected to EAE or Lysolecithin injury. We determined that while loss of Fibuin-2 did not affect the initial course of EAE, subsequent recovery after acquiring peak clinical severity was better in the Fibulin-2 heterozygote or homozygote null animals. Thus, the loss of Fibulin-2 improved recovery implying that Fibulin-2 elevation in EAE is detrimental for recovery. We have since determined that the better recovery in Fibulin-2 deficient mice is due to increased oligodendrogenesis and remyelination. Similar data sets were obtained in the Lysolecithin-demyelination model, in which there were more oligodendrogenesis and remyelination profiles in animals that were genetically deficient for Fibulin-2.

We resolved next to identify the molecular mechanisms of Fibuilin-2 as an inhibitor of oligodendrogenesis. To this end, we conducted single-cell RNA sequencing of the spinal cord of wild-type or Fibulin-2 deficient mice during EAE. Analysis shows lack of myelin genes and also increased death signatures in cells from wild type compared to Fibulin-2 null animals. These results suggest that the presence of Fibullin-2 and its upregulation in EAE kills oligodendrocytes making them less available for remyelination. To affirm this, we did real time imaging studies in tissue culture and observed that when oligodendrocytes were maturing in the presence of Fibulin-2 they die by activating a NOTCH signalling cascade within them. Thus, Fibulin-2 is a death signal acting via the NOTCH signaling pathway, to kill oligodendrocytes during their maturation resulting in impeding the process of myelin repair following injury.

Altogether, in year 1, we have made prominent progress in affirming the elevation of Fibulin-2 in MS, in defining a mechanism for the inhibitory roles of Fibulin-2, and of showing in genetically deficient mice that the loss of Fibulin-2 results in better clinical recovery. We have therefore identified Fibulin-2 as a new inhibitor that we would need to overcome for successful repair in MS.

The substantial progress has been written up in a manuscript that is currently in submission. The manuscript is included here.

- **What opportunities for training and professional development has the project provided?**

  The grant has provided significant training opportunities and professional development for trainees. Dr. Samira Ghorbani, a postdoctoral fellow, led the work where she oversaw the entire project, conducted experiments in EAE in Fibulin-2 null mice, and where she then wrote the manuscripts with editing from the Principal Investigator. This professional development therefore encompassed training in details of experiments, planning and execution, interpretation of data, and writing of the manuscript, besides of being in charge of a number of other individuals pivotal to this work. The grant also offered opportunities of small roles (conducting specific experiments) for three graduate students, Cenxiao Li, Brian Lozinski, and Dorsa Moezzi. Iin this regard, Cenxiao

Li evaluated how Fibulin-2 is generated by astrocytes, Brian Lozinski conducted Lysolecithin surgery, and Dorsa Moezzi helped with the EAE experiments. These graduate students therefore learned not only particular aspects of their work but also how to integrate their data into a more comprehensive and overarching story to complete the understanding of Fibulin-2 in MS. The grant also offered opportunity to another postdoctoral fellow, Dr. Yifei Dong, who together with Dr. Ghorbani, trained under a bioinformatics specialist, Dr. Charlottee D'Mello, and learned mining of single cell RNA databases, and how to move on from those datasets. Thus, learning opportunities for students were substantial. This has also resulted in professional development and progress as Dr. Ghorbani has accepted an Assistant Professorship at the University of Toronto from January 2024 and Dr. Yifei Dong located to the University of Saskatchewan in the past year to take up an Assistant Professorship position.

- **How were the results disseminated to communities of interest?**

  The results have been written up into a manuscript that is in consideration of publication at an international peer-reviewed journal. This would be disseminated to the scientific community of the datasets that we have obtained. Moreover, Dr. Ghorbani had the opportunity to present results at the ACTRIMS meeting (February 2023, San Diego), the largest meeting on MS in North America. Dr. Ghorbani will also be presenting at the forthcoming International Congress of Neuroimmunology in Quebec City (Aug 20-25, 2023). Dr. Yong intends to present part of these results to the lay MS community in his dissemination of results to the public in September 2023.

-
- **What do you plan to do during the next reporting period to accomplish the goals?**

  During the next reporting period, we will focus on the combination of disrupting both fibulin-2 and another inhibitor of oligodendrogenesis, versican, to address whether targeting two prominent inhibitors would result in a much more pronounced regenerative events than affecting one alone. This combination treatment will shed light on clinical translation on whether it will be necessary to affect multiple inhibitors or if affecting one is adequate.

Impact -

The impact of the project is substantial. We have identified a new inhibitor of oligodendrogenesis and myelin repair in lesions. The results indicate that one needs to develop means to overcome Fibulin-2 in order for successful regeneration of lesions in Multiple Sclerosis to occur. This should also spawn a new area of developing drugs in order to overcome Fibulin-2 inhibitory roles. It is hoped that a means to overcome Fibulin-2 can be brought in the future into a clinical trial in MS in order to foster regeneration.

- **What was the impact on the development of the principal discipline(s) of the project?**

  Nothing to report

- **What was the impact on other disciplines?**

  In the manuscript that is in submission, we point out that Fibulin-2 is also elevated in Alzheimer's Disease, Stroke, and traumatic brain injury. We would anticipate that the elevated Fibulin-2 in these conditions, and likely many other neurological conditions, would similarly impede repair processes. Thus, the data from this MS-focused work has wide-reaching implications in other areas of neurology.

- **What was the impact on technology transfer?**

At this point, we have not developed any medications to overcome Fibulin-2 although that would be one of our intentions. Thus, there is no immediate impact on technology transfer at this point although we hope that will change in the future.

- **What was the impact on society beyond science and technology?**

  The impact on society would be on having identified an inhibitor of repair processes and recovery from neurological conditions. Neurological conditions afflict a substantial portion of the population and are often long-lingering diseases with huge societal and financial implications. If Fibulin-2 could be overcome for regenerative and recovery processes this will have a positive impact on society.

Changes/Problems -

No changes in approach or intent of proposal. Thus, there is nothing to report in this section.

Products –

Publications, conference papers, and presentations

- **Journal publications.**

  The manuscript being submitted is enclosed here for your reference.

- **Books or other non-periodical, one-time publications.**

  Nothing to report

- **Other publications, conference papers, and presentations.**

  Nothing to report

- **Website(s) or other Internet site(s)**

  Nothing to report

- **Technologies or techniques**
- Nothing to report
- **Inventions, patent applications, and/or licenses**

  Nothing to report

- **Other Products**

  Nothing to report

- **Participants & Other Collaborating Organizations - What individuals have worked on the project?**

Name:	Samira Ghorbani
Project Role:	Postdoctoral fellow
Researcher Identifier (e.g. ORCID ID):	
Nearest person month worked:	12 months per year
Contribution to Project:	Dr. Samira Ghorbani, a postdoctoral fellow, led the work where she oversaw the entire project, interpreted the data and planned the next steps, conducted experiments in EAE in Fibulin-2 null mice, and where she then wrote the manuscripts with editing from the Principal Investigator.

	She was also in charge of a number of other individuals pivotal to this work
Funding Support:	Canadian Institutes of Health Research postdoctoral fellowship plus stipend from this DOD grant
Name:	*Kathleen Hagen*
Project Role:	*Research Technician*
Researcher Identifier (e.g. ORCID ID):	
Nearest person month worked:	12 months per year
Contribution to Project:	Ms. Hagen isolated, cultured and maintained oligodendrocytes in culture and tested and documented their responses to fubulin-2. She also performed animal EAE experiments under the supervision of Dr. Ghorbani.
Funding Support:	This DOD grant

- **Has there been a change in the active other support of the PD/PI(s) or senior/key personnel since the last reporting period?**

  No change

- **What other organizations were involved as partners?**

  None

Special Reporting Requirements

Appendices -

See attached manuscript submitted for peer review. This contains data.
Title: Lesional fibulin-2 promotes death to impede oligodendrocyte maturation.

Lesional fibulin-2 promotes death to impede oligodendrocyte maturation

Samira Ghorbani[1], Cenxiao Li[1], Brian M. Lozinski[1], Dorsa Moezzi[1], Charlotte D'Mello[1], Yifei Dong[1,2], Frank Visser[1], Hongmin Li[1,3], Claudia Silva[1], Mengzhou Xue[3], V. Wee Yong[1] *

[1]Hotchkiss Brain Institute and Department of Clinical Neurosciences, University of Calgary, Canada

[2] Department of Biochemistry, Microbiology, & Immunology, College of Medicine, University of Saskatchewan, Canada

[3]Department of Cerebrovascular Diseases, The Second Affiliated Hospital of Zhengzhou University, Zhengzhou, China

*Author for correspondence: vyong@ucalgary.ca and 1-403-2203544

Abstract (200 words): Impairment of oligodendrocytes and myelin contributes to neurological disorders including multiple sclerosis (MS), stroke and Alzheimer's disease[1-4]. Regeneration of myelin (remyelination) decreases the vulnerability of demyelinated axons[1,5,6] but this repair process commonly fails with disease progression[7-9]. A contributor to inefficient remyelination is the altered extracellular matrix (ECM) in lesions[10-12] that remains to be better defined. We have identified fibulin-2 (FBLN2) as a highly upregulated ECM component in lesions of MS and stroke, and in proteome databases of Alzheimer's disease[13] and traumatic brain

injury[14]. Focusing on MS, the inhibitory role of FBLN2 was suggested in the experimental autoimmune encephalomyelitis (EAE) model in which genetic FBLN2 deficiency alleviated disease severity. Single-cell RNA sequencing of EAE-afflicted spinal cord with FBLN2-deficiency showed higher number of myelinating oligodendrocytes, corroborated by microscopy in EAE or lysolecithin-induced demyelination. Mechanistically, FBLN2 killed oligodendrocyte progenitor cells during their maturation to oligodendrocytes by engaging the Notch pathway. Targeted adeno-associated virus-deletion of FBLN2 in astrocytes improved oligodendrocyte numbers and functional recovery in EAE and generated new myelin profiles in myelin-reporter mice after lysolecithin demyelination. Collectively, our findings implicate FBLN2 as a hitherto unrecognized injury-elevated ECM, and a novel therapeutic target, that impairs oligodendrocyte maturation and myelin repair.

Main:

The importance of oligodendrocytes and myelin in the central nervous system (CNS) is evidenced by the neuronal dysfunction and physical disability observed following their damage[1]. Oligodendrocyte loss and myelin impairment contribute not only to classic demyelinating disorders such as MS, but also to dystonias, stroke, neurodegenerative conditions such as Alzheimer's disease, and even in cognitive dysfunctions[2,3,15,16]. In preclinical studies, the generation of new oligodendrocytes and myelin is important for motor skill learning and memory[17,18].

Remyelination is a repair response to myelin loss and it protects denuded axons from irreversible degeneration as manifested by preserved axon density[6], decreased loss of thalamic volume[1] and low disability scores[19]. Strategies to enhance remyelination such as overcoming impediments to repair are sought after[20,21].

Remyelination begins with the recruitment and differentiation/maturation of oligodendrocyte progenitor cells (OPCs) to myelin-forming oligodendrocytes[9,20]. Remyelination may occur extensively at early stages of MS, but it often fails contributing to progression of disability[7,8,19]. While OPC numbers may not be reduced in many MS lesions, their maturation to oligodendrocytes and hence oligodendrocyte number is often deficient[21,22]. Identifying and overcoming factors that impair oligodendrocyte maturation are of interest.

One contributor to inefficient remyelination is the altered ECM in lesions[10,11]. While the ECM is a normal constituent of the CNS in its basement membranes, perineuronal net and in the neural interstitial matrix[23], the excessive deposition and accumulation of ECM members such as the chondroitin sulfate proteoglycans (CSPGs) inhibit axonal regeneration in traumatic CNS injuries[24]. We described that the CSPG member, versican-V1, deposited in MS lesions impedes OPC properties and remyelination[25]. Moreover, the dysregulated ECM may affect immune responses in lesions[10,26] and thereby prevent the regeneration of oligodendrocytes and myelin. While there are more than 300 ECM core proteins, only a minority have been characterized in neurological injuries.

Prominent elevation of FBLN2 in CNS lesions

To gain a thorough overview of the altered ECM in CNS injuries, we first interrogated available proteomic databases for MS and EAE. FBLN2 was qualitatively elevated in MS[27] and by 9.5 fold[28] in the quantitative EAE proteome library (Extended Data Fig.1a). As FBLN2 is minimally described in the CNS, with roles in synapse formation/neurogenesis[29] and elevated immunoreactivity but unknown functions in astrocytes after traumatic CNS injury[30], we sought to interrogate FBLN2 further.

Frozen brain autopsy specimens from five people with MS were analysed for lesions by loss of luxol fast blue (LFB) myelin staining and by prominent accumulation of $CD45^+$ immune cells. Three MS cases (MS-352, MS-230, MS-338) had white matter lesions characterized by uniform distribution of $CD45^+$ immune cells throughout the lesion (active) or in the hypercellular edge (chronic active lesion). FBLN2 immunoreactivity was markedly elevated in active and chronic active lesions, and in the inactive core, but not in normal appearing white matter (NAWM) (Fig. 1a, b) or in two additional MS cases without lesions in the section examined (data not shown).

Next, we assessed FBLN2 expression in spinal cord white matter lesions in both EAE and lysophosphatidylcholine (LPC, lysolecithin)-induced demyelination models. FBLN2 was accumulated in myelin basic protein (MBP)-deficient demyelinated EAE lesions at the peak (day 18) and post peak (day 40) stages of clinical severity (Fig.1c-e). Using Imaris 3D rendering, FBLN2 was found extracellularly or colocalized to glial fibrillary acidic protein (GFAP)-positive astrocytes (Fig.1f). This was corroborated by in vitro data of increased FBLN2 in activated astrocytes (Extended Data Fig. 1b, c). Moreover, upregulation of FBLN2 persisted at different time points in lysolecithin-demyelinated lesions (Fig.1g, h).

To evaluate whether FBLN2 is elevated across neurological disorders, we selected hemorrhagic stroke with a different origin (hematoma) from MS. In murine samples from collagenase-induced intracerebral hemorrhage (ICH) and also in human hemorrhagic stroke, prominent accumulation of FBLN2 was noted (Extended Data Fig. 1d-f). Furthermore, interrogating publicly available proteomic datasets revealed elevation of FBLN2 in Alzheimer's Disease[13], suggesting that FBLN2 upregulation is common in CNS injuries. While not highlighted by the original authors, our datamining shows higher levels of FBLN2 in the cerebrospinal fluid after severe traumatic brain injury and of people with Alzheimer's Disease compared to controls[14,31].

Course of EAE in FBLN2 deficient mice

To better understand the role of FBLN2 in CNS injury and neuroinflammation, EAE was induced in 10–12-week-old C57BL/6 wildtype (WT) and FBLN2 deficient mice; the latter included heterozygous (*Fbln2+/-*) (Het) and homozygous (*Fbln2-/-*) (Homo) mice. The severity of EAE did not differ at the initial inflammatory stage of disease (Fig. 2a, b), likely due to the lack of activity of FBLN2 on immune cells as informed by macrophage cytokine production or T cell proliferation in culture (Extended Data Fig. 2a-f). However, clinical disability scores improved statistically, albeit marginally, in FBLN2 deficient mice post peak of clinical severity (Fig. 2a, c); this is the period in which regeneration of oligodendrocytes and myelin leads to a modest decline (as immune activity is still prominent) in EAE disability as noted by others[32]. We did not observe differences between *Fbln2+/-* and *Fbln2-/-* mice (Fig. 2a-c).

Single-cell RNA sequencing (scRNA-seq) links myelinating oligodendrocytes and FBLN2 inversely

To delineate the underlying reasons for better functional recovery from EAE in FBLN2 deficient mice, scRNA-seq was performed on spinal cords from WT or FBLN2 Het and Homo knockout mice (3 mice per group) post-peak EAE (day 18). Unsupervised integrated alignment of all 34,395 cells from the 9 spinal cords delineated 17 clusters which were present in all experimental groups (Fig. 2d, e). Cell population analyses revealed changes in cellular composition of spinal cords and particularly of more oligodendrocytes in FBLN2 deficient mice compared to WT group (Fig. 2e, i). Lineage cell markers identified clusters 4 and 12 as oligodendrocyte lineage cells (*Plp1, Ptgds, Nkain2, Apod, Aplp1, Klk6 Mog, Mbp, Mag, Olig1/2*) (Supp Table 1 and Extended Data Fig. 3a, b). Oligodendrocytes from FBLN2 deficient mice displayed higher levels of myelination related genes including *Nrdg1*, *Myrf*, *Bcas1*, *Opalin, Gpr37, Smad7, Fgfr2, Cnp, Mog, Mbp, Mag and Plp1* genes[20,33] (Fig. 2f, g and Supp Table 2).

Next, 523 differentially expressed genes (DEG) in oligodendrocyte lineage cells between FBLN2 deficient mice vs. WT were analyzed using ingenuity pathway analysis (IPA). Pathways such as ferroptosis and neuroinflammation were enriched in oligodendrocytes from WT mice, whereas myelination signaling as well as other pathways with pro-myelination properties including cAMP-mediated, CREB, FAK /integrin, CXCR4, and IL-8 signaling were enriched in FBLN2 deficient mice[33-36] (Fig. 2h).

Oligodendrocyte lineage clusters from the 3 experimental groups totalling 2592 cells were subset and re-clustered demonstrating 7 subclusters (Fig. 2i). Subclusters 0, 1 and 2 presented several markers of mature oligodendrocytes (MOL) identified by

previous studies[37,38] including *Ptgds, Il33, Klk6, Myrf, Plp1, Mog, and Spock1*. Although these subclusters shared the same transcriptional profile, interferon (IFN) response genes (e.g., *Ifit3*, *Stat1 and Irf1) and* genes necessary for antigen presentation (*Psmb8/9, Tap1/2*) were enriched in subcluster 2 (IFN-MOL). Unique expression of markers previously identified in disease associated oligodendrocytes (DA-MOL) was found in subcluster 0 (e.g., *C4b*, S*erpina3n, Plin3 and Anax5)*. Subcluster 3 and 4 showed higher levels of inflammation and oxidative stress genes such as *S100b*, *S100a1/8/9*, *C1qa, Lyz2, Ftl*, *Tf* and *Cyba/b* (Stressed-OL). Subcluster 5 displayed OPC markers (*Sox6, Ptprz1, Pdgfra and Vcan) as well as* markers of committed OPC (COP) such as *Bcas1, Gpr17 and Mylk.* Subcluster 6 was annotated as newly formed oligodendrocytes (NFOL) as they expressed *Prom1, Rras2, Bcas1* and higher levels of myelin genes (Fig. 2j, Extended Data Fig. 3c, d and Supp Table 3).

MOL and DA-MOL constituted the majority of oligodendrocyte population in FBLN2 deficient mice while stressed-OLs were more abundant in WT mice (Fig. 2k). Total number of COPs, NFOLs and MOL (myelinating oligodendrocytes) was significantly higher in FBLN2 knockout mice (Fig. 2l).

COP, NFOL and MOL subclusters (5, 6, and 1) were predicted by IPA to be involved in myelination through upregulation of synthesis of lipid, organization of cytoskeleton, synaptogenesis, axon ensheathment and other pathways such as CREB, neuregulin, CXCR4, IL-8, IL-33 and mTOR signaling[33-36,39-41] (Fig. 2m, Extended Data Fig. 3e). On the other hand, DA-MOL, IFN-MOL and stressed oligodendrocytes (subclusters 0, 2, 3 and 4) had an altered gene expression pattern in the modules predicted to promote cell death, ferroptosis, oxidative stress and neuroinflammation (Fig.

2m). Our findings highlight the significance of COPs, NFOLs and MOLs as myelinating oligodendrocytes that were expanded in FBLN2 deficient mice with better clinical recovery from EAE.

FBLN2 deficient mice have more mature oligodendrocytes in EAE and lysolecithin injuries

To confirm findings from scRNA-seq, immunofluorescence staining was performed on longitudinal spinal cord sections of EAE mice (from Fig. 2a at sacrifice) to assess oligodendrocyte lineage cells. Despite the comparable extent of demyelination and inflammation (Fig. 3a-d), consistent with the lack of obvious effects of FBLN2 on immune cells (Extended Data Fig. 2e-j), FBLN2 Homo and Het knockout mice showed an increase in number of mature oligodendrocytes ($Olig2^+CC1^+$) within lesions. The number of OPCs ($Olig2^+PDGFR\alpha^+$) remained unchanged (Fig. 3e, h-j).

In corroboration of the EAE results, coronal spinal cord sections analyzed 14 days after lysolecithin demyelination showed that FBLN2-deficient mice had a higher number of mature oligodendrocytes within the lesion while OPCs remained the same (Fig. 3f, g, K-m). Collectively, the EAE and lysolecithin results affirm the scRNAseq data that loss of FBLN2 increases the number of mature oligodendrocytes following demyelination.

FBLN2 kills OPCs during their maturation to oligodendrocytes

To define the properties of FBLN2 on oligodendrocytes, we isolated and plated OPCs onto a FBLN2 substrate in differentiation medium. While it did not affect initial adhesion, FBLN2 was strongly inhibitory for maturation of both human and mouse OPCs

to oligodendrocytes. As OPCs differentiate, they extend their processes as a prerequisite for myelin enwrapment of axons in vivo, and they upregulate expression of sulfatide O4 and myelin proteins (e.g., MBP, MAG) while downregulating PDGFRα[20]. FBLN2 reduced process outgrowth and proportion of O4 and MBP-expressing cells (Fig. 4a-e, l, m). In contrast, other members of the FBLN family including FBLN1 and FBLN3 were not inhibitory (Fig. 4f, g).

Live imaging of OPCs showed that the initial attachment and process extension of OPCs were not affected by plating onto FBLN2; however, subsequent cell density, maturation to $O4^+$ oligodendrocytes and process outgrowth declined noticeably after 12h (Fig. 4h-k and Extended Data Fig. 4a, b). In contrast to oligodendrocytes, FBLN2 did not affect neuronal survival (Extended Data Fig. 2g-j).

To address whether FBLN2 hinders OPC proliferation, cells were grown in proliferation medium supplemented with growth factors necessary for OPC proliferation (PDGF and FGF). Dividing OPCs were labelled with 5-ethynyl-2'-deoxyuridine (EdU) for 6h before detection of the incorporated EdU. The percentage of proliferating OPCs did not change in the presence of FBLN2 (Extended Data Fig. 4c, d). Strikingly, when OPCs were cultured in differentiation medium so that they could mature to oligodendrocytes, FBLN2 induced a G0/G1 phase cell cycle arrest detected by flow cytometry (Extended Data Fig. 4e, f).

To examine whether FBLN2 induces apoptosis in differentiating OPCs, live imaging of OPCs plated on control and FBLN2 substrates was performed in the presence of propidium iodide (PI) in the differentiation culture medium. Few OPCs incorporated PI as a sign of cellular compromise during the first hours of observation, whereas PI uptake

was significantly increased in FBLN2-exposed cells after 12h (Fig. 4n, o). Moreover, real-time PCR gene expression analysis of pro-apoptotic Bax and anti-apoptotic Bcl-2 molecules from differentiating-OPCs showed an increase in the Bax/Bcl2 ratio following FBLN2 exposure for 6h (Fig. 4p).

Collectively, these results highlight that FBLN2 does not affect OPC proliferation, but it induces cell death in differentiating (committed) OPCs.

FBLN2 engages notch signaling to impede oligodendrocyte maturation

To investigate the mechanisms of FBLN2, mouse OPCs were plated on uncoated or FBLN2 coated wells in differentiation media for 6h. Bulk RNA sequencing was performed to identify up- or down-regulated genes (Fig. 5a, b). IPA analysis on DEGs by FBLN2-exposed OPCs highlighted the enrichment of apoptosis and Notch signaling pathways while cell cycle regulation as well as actin/microtubule cytoskeleton signaling were downregulated (Fig. 5c and Extended Data Fig. 4g). FBLN2 exposure inhibited various myelination-related signaling pathways known to promote oligodendrogenesis including mTOR, TGF-β, PI3K/AKT, MAPK, IL-8 and CXCR4 pathways[33-36, 41](Extended Data Fig. 4g). Several cell cycle-related genes as well as pro- or anti-apoptotic genes *such Ccnd1, Cdkn1α, caspase 9, Krt18, Birc3, Timp-1, Cflar* and *Bcl2* family were dysregulated in FBLN2-exposed OPCs (Extended Data Fig. 4h); these likely contribute to the death observed above when OPCs were differentiating to oligodendrocytes in the presence of FBLN2.

The RNA sequencing dataset showed that Notch signaling was enriched in differentiating-OPCs cultured on FBLN2 substrate (Fig. 5c). NOTCH proteins are

transmembrane proteins activated by ligands such as jagged1. Ligand engagement results in the proteolytic cleavage of the NOTCH receptor and release of its intracellular domain NICD that translocates to the nucleus to induce expression of target genes such as *Hes5* [42]. Notch signaling has been shown to induce growth arrest and apoptosis[42,43]. Thus, we hypothesized that FBLN2 activates Notch signaling in differentiating-OPCs, resulting in maturation block and cell death. In support, pharmacological inhibition of Notch signaling (SAHM1, 10 μM, 24h) overcame FBLN2-mediated reduction of $O4^+$ cell numbers and extent of their process formation (Fig. 5g-i). In addition, genetic manipulation using two *Notch1* siRNAs (200 nM) reversed the differentiation block of FBLN2 and increased the number of $O4^+$ oligodendrocytes after 24h (Fig. 5g). In accordance with RNAseq findings, higher levels of NICD were shown in OPCs plated on FBLN2 substrate using western blot analysis (Extended Data Fig.4i, j). Finally, we used a Notch pathway luciferase reporter assay to measure functional Notch activity in response to FBLN2. Relative luciferase activity (Firefly to Renilla luminescence) increased significantly in Hek239 cells transfected with CSL (CBF1/RBP-Jk) luciferase reporter following FBLN2 (10 μg/ml) treatment, validating Notch activation by FBLN2 (Fig. 5h, i).

The tissue culture results were corroborated in vivo. According to scRNA-seq dataset, Notch signaling was present in COP subcluster that can be considered equivalent to differentiating OPCs in culture (Fig. 5j). Some of Notch-related genes (*Maml2, Rbpj*) showed an upward trend in WT mice (Fig. 5k), however, it did not reach statistical significance due to the small size of this population especially in WT mice. Notch activation in oligodendrocytes of MS lesions was confirmed by immunolabeling for

NICD (Fig. 5l). Immunofluorescence staining of spinal cord from EAE mice as well as lysolecithin-lesions showed a smaller population of oligodendrocytes expressing Hes5 or cleaved caspase 9 in FBLN2 deficient mice (Extended Data Fig. 5e-m). Moreover, less Notch activity and lower amount of cleaved caspase 9 were detected by western blot analysis of spinal cord lysates from FBLN2 KO mice (Extended Data Fig. 5n-q).

While our findings suggest that FBLN2 impairs oligodendrogenesis through engaging the Notch signaling pathway, the involvement of other pathways is not ruled out. When OPCs were exposed to inhibitors of several signaling pathways known to affect oligodendrogenesis[33,41], we found that an inhibitor to ROCK and MEK/ERK, but not to P38MAPK , PI3-K/AKT/mTOR, Wnt/β-catenin , Src/Syk , BMP4 or Smad3 signaling, rescued the FBLN2 inhibition of process formation at 24h (Extended Data Fig. 6a-h).

Reducing FBLN2 levels by AAV promotes maturation of oligodendrocytes and myelin profiles

To overcome the effects of injury-induced elevation of FBLN2 in the CNS, AAV-coupled CRISPR/Cas9 system was used to target its expression in astrocytes given the expression of FBLN2 in this population (Fig. 1e, Extended Data Fig. 1b, c) [30,44]. We generated 2 different AAVs: 1) recombinant PHPeB AAV vector packaging a specific gRNA for targeted disruption of FBLN2 (U6-Fbln gRNA-GFAP-eGFP), and 2) Recombinant PHPeB AAV vector encoding Cas9 under the control of a GFAP promoter (GFAP-SaCas9-HAFLAGHA) (Fig. 6a). AAVs ($3x10^{11}$ viral genomes (vg) per virus) were co-delivered retro-orbitally to mice 2 weeks before EAE induction or lysolecithin injection.

Mice were injected with AAV encoding non-target guide RNA (U6-Luc gRNA-GFAP-eGFP) as control. Transduction efficiency ranged between 30-40 % in both astrocyte culture and in vivo experiment (Extended Data Fig. 7a-d). Our data showed the specificity, feasibility and success of this approach to lower FBLN2 levels in vitro and in vivo (Extended Data Fig. 7e-j, Fig. 6e, f, k, n). Astrocyte-specific FBLN2 knockdown (KD) reduced average EAE daily score during post peak of clinical severity (Fig. 6b-d). Although the extent of demyelination and inflammation remained unchanged (Fig. 6 g, o, p), astrocytic deletion of FBLN2 increased the number of mature oligodendrocytes in EAE (Fig. 6h-j) or lysolecithin lesions (Fig. 6l, m, q, r).

Finally, to identify the newly formed oligodendrocytes and myelin sheaths, NG2 Cre^{ER}:$MAPT^{mGFP}$ mice were used where GFP expression indicates new oligodendrocytes and myelin[18,25,32] (Fig. 6s). Analyses were conducted in the lysolecithin model as the area of de- and remyelination in the ventral white matter of the spinal cord was defined by the deposition of toxin. NG2 Cre^{ER}:$MAPT^{mGFP}$ mice received AAVs 2 weeks before lysolecithin-surgery. GFP cassette was removed from the AAV vector to avoid interference with GFP signal from newly formed oligodendrocytes. FBLN2 deletion in astrocytes resulted in larger area of GFP within the lysolecithin lesions 14 dpi, and cells with profuse myelin profiles could be observed (Fig. 6t, u). Thus, reducing lesional FBLN2 improves oligodendrogenesis which is associated with better functional recovery in EAE, and new myelin profiles in lysolecithin injury.

Discussion

The altered ECM microenvironment of CNS lesions is a relatively understudied area even though ECM components affect cells in profound ways. Commonly described ECM in CNS lesions include CSPGs, fibronectin and laminins but these constitute a minority of >300 ECM core proteins. Here, we implicate a new ECM component existent in CNS lesions with prominent inhibitory effects on maturation of oligodendrocytes from OPCs, an important step in remyelination to restore functions in the CNS. FBLN2 is distinct functionally from CSPGs in that it does not obviously affect neuronal or immune cells (Extended Data Fig.2), and it does not affect the initial attachment of OPCs unlike CSPGs[25]. However, FBLN2 impedes the maturation of oligodendrocytes from OPCs, considered to be the prominent block[45] in remyelination after adult CNS injuries. That FBLN2 is elevated and persistent in active and inactive lesions of MS (Fig. 1a, b), intracerebral hemorrhage of stroke (Extended Data Fig.1 d-f) and in our datamining of traumatic brain injury and Alzheimer's disease library[13,14,31], and likely other neurological conditions, highlight the need to consider and counter this ECM component after CNS injuries.

In our study, we did not find differences between *Fbln2*+/- and *Fbln2*-/- mice. Thus, the loss of a single allele overcome the defect in formation of mature oligodendrocytes after demyelination which was not enhanced by loss of the second allele. This suggests that there are additional inhibitory molecules within the lesion, such as CSPGs, as well as compensatory mechanisms in response to complete loss of FBLN2, which masks the difference between heterozygous and homozygous mice.

Outside of the CNS, FBLN2 is mainly expressed in connective tissues where it functions as intramolecular bridges that provide stability to ECM structures[46,47]. Whether

FBLN2 deposition in CNS lesions is aimed at stabilizing injury-induced ECM deposition is unknown.

That FBLN2 engages Notch signaling in OPCs is significant, as Notch1 engagement by its ligand Jagged1 on axons of retinal ganglion cells prevents premature OPC maturation and thus controls the timely appearance of oligodendrocytes in optic nerve development[43]. Notch1 signaling has been reported in MS lesions where Jagged1 of reactive astrocytes interacts with Notch1 on OPCs[48]; this limited OPC differentiation to oligodendrocytes via transcription factor HES5, which competes with SOX10 to block MBP expression[48]. Subsequent studies showed that blocking Notch signaling attenuated EAE severity and improved myelin repair[49]. Moreover, Notch deficiency in OPCs promoted remyelination in lysolecithin and cuprizone models of demyelination[50,51]. To these results, we now add FBLN2 as an injury-enhanced trigger for Notch inhibition of OPC differentiation in MS and likely other neurological conditions (Extended Data Fig. 8).

In summary, we have identified a hitherto unknown inhibitor of oligodendrogenesis and myelin repair. Overcoming FBLN2 has the therapeutic potential not only in MS but also in other conditions in which myelin impairment contributes to axonal dysfunction and cognitive decline.

References:

1 Lubetzki, C., Zalc, B., Williams, A., Stadelmann, C. & Stankoff, B. Remyelination in multiple sclerosis: from basic science to clinical translation. *Lancet Neurol* **19**, 678-688 (2020). https://doi.org:10.1016/S1474-4422(20)30140-X

2 Depp, C. *et al.* Myelin dysfunction drives amyloid-β deposition in models of Alzheimer's disease. *Nature* **618**, 349-357 (2023). https://doi.org:10.1038/s41586-023-06120-6

3 Blanchard, J. W. *et al.* APOE4 impairs myelination via cholesterol dysregulation in oligodendrocytes. *Nature* **611**, 769-779 (2022). https://doi.org:10.1038/s41586-022-05439-w

4 Pintér, P. & Alpár, A. The Role of Extracellular Matrix in Human Neurodegenerative Diseases. *Int J Mol Sci* **23** (2022). https://doi.org:10.3390/ijms231911085

5 Fünfschilling, U. *et al.* Glycolytic oligodendrocytes maintain myelin and long-term axonal integrity. *Nature* **485**, 517-521 (2012). https://doi.org:10.1038/nature11007

6 Irvine, K. A. & Blakemore, W. F. Remyelination protects axons from demyelination-associated axon degeneration. *Brain* **131**, 1464-1477 (2008). https://doi.org:10.1093/brain/awn080

7 Yong, H. Y. F. & Yong, V. W. Mechanism-based criteria to improve therapeutic outcomes in progressive multiple sclerosis. *Nat Rev Neurol* **18**, 40-55 (2022). https://doi.org:10.1038/s41582-021-00581-x

8 Goldschmidt, T., Antel, J., König, F. B., Brück, W. & Kuhlmann, T. Remyelination capacity of the MS brain decreases with disease chronicity. *Neurology* **72**, 1914-1921 (2009). https://doi.org:10.1212/WNL.0b013e3181a8260a

9 Franklin, R. J. M. & Simons, M. CNS remyelination and inflammation: From basic mechanisms to therapeutic opportunities. *Neuron* **110**, 3549-3565 (2022). https://doi.org:10.1016/j.neuron.2022.09.023

10 Ghorbani, S. & Yong, V. W. The extracellular matrix as modifier of neuroinflammation and remyelination in multiple sclerosis. *Brain* (2021). https://doi.org:10.1093/brain/awab059

11 van Schaik, P. E. M., Zuhorn, I. S. & Baron, W. Targeting Fibronectin to Overcome Remyelination Failure in Multiple Sclerosis: The Need for Brain- and Lesion-Targeted Drug Delivery. *Int J Mol Sci* **23** (2022). https://doi.org:10.3390/ijms23158418

12 Segel, M. *et al.* Niche stiffness underlies the ageing of central nervous system progenitor cells. *Nature* **573**, 130-134 (2019). https://doi.org:10.1038/s41586-019-1484-9

13 Bai, B. *et al.* Correction to: Proteomic landscape of Alzheimer's Disease: novel insights into pathogenesis and biomarker discovery. *Mol Neurodegener* **16**, 72 (2021). https://doi.org:10.1186/s13024-021-00493-w

14 Shultz, S. R. *et al.* Temporal proteomics of human cerebrospinal fluid after severe traumatic brain injury. *J Neuroinflammation* **19**, 291 (2022). https://doi.org:10.1186/s12974-022-02654-0

15 Yellajoshyula, D., Pappas, S. S. & Dauer, W. T. Oligodendrocyte and Extracellular Matrix Contributions to Central Nervous System Motor Function: Implications for Dystonia. *Mov Disord* **37**, 456-463 (2022). https://doi.org:10.1002/mds.28892

16 Remer, J. *et al.* Longitudinal white matter and cognitive development in pediatric carriers of the apolipoprotein ε4 allele. *Neuroimage* **222**, 117243 (2020). https://doi.org:10.1016/j.neuroimage.2020.117243

17 McKenzie, I. A. *et al.* Motor skill learning requires active central myelination. *Science* **346**, 318-322 (2014). https://doi.org:10.1126/science.1254960

18 Pan, S., Mayoral, S. R., Choi, H. S., Chan, J. R. & Kheirbek, M. A. Preservation of a remote fear memory requires new myelin formation. *Nat Neurosci* **23**, 487-499 (2020). https://doi.org:10.1038/s41593-019-0582-1

19 Bodini, B. *et al.* Dynamic Imaging of Individual Remyelination Profiles in Multiple Sclerosis. *Ann Neurol* **79**, 726-738 (2016). https://doi.org:10.1002/ana.24620

20 Plemel, J. R., Liu, W. Q. & Yong, V. W. Remyelination therapies: a new direction and challenge in multiple sclerosis. *Nat Rev Drug Discov* **16**, 617-634 (2017). https://doi.org:10.1038/nrd.2017.115

21 Gharagozloo, M., Bannon, R. & Calabresi, P. A. Breaking the barriers to remyelination in multiple sclerosis. *Curr Opin Pharmacol* **63**, 102194 (2022). https://doi.org:10.1016/j.coph.2022.102194

22 Kuhlmann, T. *et al.* Differentiation block of oligodendroglial progenitor cells as a cause for remyelination failure in chronic multiple sclerosis. *Brain* **131**, 1749-1758 (2008). https://doi.org:10.1093/brain/awn096

23 Lau, L. W., Cua, R., Keough, M. B., Haylock-Jacobs, S. & Yong, V. W. Pathophysiology of the brain extracellular matrix: a new target for remyelination. *Nat Rev Neurosci* **14**, 722-729 (2013). https://doi.org:10.1038/nrn3550

24 Tran, A. P., Warren, P. M. & Silver, J. New insights into glial scar formation after spinal cord injury. *Cell Tissue Res* **387**, 319-336 (2022). https://doi.org:10.1007/s00441-021-03477-w

25 Ghorbani, S. *et al.* Versican promotes T helper 17 cytotoxic inflammation and impedes oligodendrocyte precursor cell remyelination. *Nat Commun* **13**, 2445 (2022). https://doi.org:10.1038/s41467-022-30032-0

26 Sutherland, T. E., Dyer, D. P. & Allen, J. E. The extracellular matrix and the immune system: A mutually dependent relationship. *Science* **379**, eabp8964 (2023). https://doi.org:10.1126/science.abp8964

27 Han, M. H. *et al.* Proteomic analysis of active multiple sclerosis lesions reveals therapeutic targets. *Nature* **451**, 1076-1081 (2008). https://doi.org:10.1038/nature06559

28 Hasan, M. *et al.* Quantitative Proteome Analysis of Brain Subregions and Spinal Cord from Experimental Autoimmune Encephalomyelitis Mice by TMT-Based Mass Spectrometry. *Proteomics* **19**, e1800355 (2019). https://doi.org:10.1002/pmic.201800355

29 Radice, P. D. *et al.* Fibulin-2 is a key mediator of the pro-neurogenic effect of TGF-beta1 on adult neural stem cells. *Mol Cell Neurosci* **67**, 75-83 (2015). https://doi.org:10.1016/j.mcn.2015.06.004

30 Schaeffer, J., Tannahill, D., Cioni, J. M., Rowlands, D. & Keynes, R. Identification of the extracellular matrix protein Fibulin-2 as a regulator of spinal nerve organization. *Dev Biol* **442**, 101-114 (2018). https://doi.org:10.1016/j.ydbio.2018.06.014

31 Bader, J. M. *et al.* Proteome profiling in cerebrospinal fluid reveals novel biomarkers of Alzheimer's disease. *Mol Syst Biol* **16**, e9356 (2020). https://doi.org:10.15252/msb.20199356

32 Mei, F. *et al.* Accelerated remyelination during inflammatory demyelination prevents axonal loss and improves functional recovery. *Elife* **5** (2016). https://doi.org:10.7554/eLife.18246

33 Wang, S., Wang, Y. & Zou, S. A Glance at the Molecules That Regulate Oligodendrocyte Myelination. *Curr Issues Mol Biol* **44**, 2194-2216 (2022). https://doi.org:10.3390/cimb44050149

34 Zhou, G. *et al*. Multifaceted Roles of cAMP Signaling in the Repair Process of Spinal Cord Injury and Related Combination Treatments. *Front Mol Neurosci* **15**,808510 (2022). https://doi.org: 10.3389/fnmol.2022.808510

35 Kadi, L. *et al.* Differential effects of chemokines on oligodendrocyte precursor proliferation and myelin formation in vitro. *J Neuroimmunol* **174**, 133-146 (2006). https://doi.org:10.1016/j.jneuroim.2006.01.011

36 Patel, J. R., McCandless, E. E., Dorsey, D. & Klein, R. S. CXCR4 promotes differentiation of oligodendrocyte progenitors and remyelination. *Proc Natl Acad Sci U S A* **107**, 11062-11067 (2010). https://doi.org:10.1073/pnas.1006301107

37 Falcão, A. M. *et al.* Disease-specific oligodendrocyte lineage cells arise in multiple sclerosis. *Nat Med* **24**, 1837-1844 (2018). https://doi.org:10.1038/s41591-018-0236-y

38 Marques, S. *et al.* Oligodendrocyte heterogeneity in the mouse juvenile and adult central nervous system. *Science* **352**, 1326-1329 (2016). https://doi.org:10.1126/science.aaf6463

39 Ljunggren-Rose, Å. *et al.* Anacardic acid induces IL-33 and promotes remyelination in CNS. *Proc Natl Acad Sci U S A* **117**, 21527-21535 (2020). https://doi.org:10.1073/pnas.2006566117

40 Kataria, H., Alizadeh, A., Karimi-Abdolrezaee, S. Neuregulin-1/ErbB network: An emerging modulator of nervous system injury and repair. *Prog Neurobiol* **180**:101643. (2019). https://doi.org: 10.1016/j.pneurobio.2019.101643

41 Shahsavani, N., Kataria, H. & Karimi-Abdolrezaee, S. Mechanisms and repair strategies for white matter degeneration in CNS injury and diseases. *Biochim Biophys Acta Mol Basis Dis* **1867**, 166117 (2021). https://doi.org:10.1016/j.bbadis.2021.166117

42 Zhou, B. *et al.* Notch signaling pathway: architecture, disease, and therapeutics. *Signal Transduct Target Ther* **7**, 95 (2022). https://doi.org:10.1038/s41392-022-00934-y

43 Wang, S. *et al.* Notch receptor activation inhibits oligodendrocyte differentiation. *Neuron* **21**, 63-75 (1998). https://doi.org:10.1016/s0896-6273(00)80515-2

44 Zhang, Y. *et al.* An RNA-sequencing transcriptome and splicing database of glia, neurons, and vascular cells of the cerebral cortex. *J Neurosci* **34**, 11929-11947 (2014). https://doi.org:10.1523/JNEUROSCI.1860-14.2014

45 Kuhlmann, T. *et al.* Differentiation block of oligodendroglial progenitor cells as a cause for remyelination failure in chronic multiple sclerosis. *Brain* **131**, 1749-1758 (2008). https://doi.org:10.1093/brain/awn096

46 Argraves, W. S., Greene, L. M., Cooley, M. A. & Gallagher, W. M. Fibulins: physiological and disease perspectives. *EMBO Rep* **4**, 1127-1131 (2003). https://doi.org:10.1038/sj.embor.7400033

47 Tsuda, T. Extracellular Interactions between Fibulins and Transforming Growth Factor (TGF)-β in Physiological and Pathological Conditions. *Int J Mol Sci* **19** (2018). https://doi.org:10.3390/ijms19092787

48 John, G. R. *et al.* Multiple sclerosis: re-expression of a developmental pathway that restricts oligodendrocyte maturation. *Nat Med* **8**, 1115-1121 (2002). https://doi.org:10.1038/nm781

49 Jurynczyk, M., Jurewicz, A., Bielecki, B., Raine, C. S. & Selmaj, K. Inhibition of Notch signaling enhances tissue repair in an animal model of multiple sclerosis. *J Neuroimmunol* **170**, 3-10 (2005). https://doi.org:10.1016/j.jneuroim.2005.10.013

50 Zhang, Y. *et al.* Notch1 signaling plays a role in regulating precursor differentiation during CNS remyelination. *Proc Natl Acad Sci U S A* **106**, 19162-19167 (2009). https://doi.org:10.1073/pnas.0902834106

51 Fan, H. *et al.* Effect of Notch1 gene on remyelination in multiple sclerosis in mouse models of acute demyelination. *J Cell Biochem* **119**, 9284-9294 (2018). https://doi.org:10.1002/jcb.27197

Methods

MS specimens

Post-mortem frozen brain tissues from people with MS were obtained from The Multiple Sclerosis and Parkinson's Tissue Bank situated at Imperial College, London (https://www.imperial.ac.uk/medicine/multiple-sclerosis-and-parkinsons-tissue-bank). This bank has been approved as a Research Tissue Bank by the Wales Research Ethics Committee (Ref. No. 18/WA/0238). Demyelinating lesions from the brains of two females (aged 50 and 42 years, MS-230 and MS-338) and one male (aged 43, MS-352) were

analyzed for this study. Lesions were not detected in two brain tissue samples from MS-234 and MS-297 (females; aged 39 and 58 years, respectively). Lesions were characterized using Luxol fast blue (LFB) and Hematoxylin & Eosin (H&E) histological stains. In addition, a combination of CD45 and MBP staining was used to determine the activity of lesions. The intracerebral hemorrhage (ICH) donor was a 70-year-old male who suffered a right middle cerebral artery infarct 5 days before death, and with a hemorrhagic transformation 2 days after. Thus, the tissue is 3 days after ICH, and collected at the Foothills Hospital at the University of Calgary. Gross examination revealed a substantial hemorrhage in the right cerebral parenchyma, along with edema and gyral flattening. The perihematomal regions and the apparently normal contralateral side were analysed. The use of all human tissues in this study has been approved by the Conjoint Health Research Ethics Board at the University of Calgary (Ethics ID REB15-0444).

Mice

All animal work was performed with ethics approval (protocol number AC21- 0174, AC21-0154, AC21-0073-4) from the Animal Care Committee at the University of Calgary under regulations of the Canadian Council of Animal Care. Fibulin-2 deficient mice (JAX 019895**)** were acquired from Jackson Laboratories as heterozygous and bred in University of Calgary Animal facility to produce wildtype, heterozygous (*Fbln2*+/) and homozygous (*Fbln2*-/-) mice. $NG2^{CreER}$ (JAX 008538) mice and membrane associated protein tau $(MAPT)^{mGFP}$ (JAX 021162) mice aged 6 to 8 weeks were acquired from Jackson Laboratories and bred in University of Calgary Animal facility to produce female $NG2^{CreER}$:$MAPT^{mGFP}$ mice. Mice were housed between 21 and 23 degrees Celsius, in low

humidity, with 12 h light and 12 h dark cycle from 7 am light and starting 7 pm dark. Female wildtype C57Bl/6 J mice (6-8 weeks old) and litters from pregnant CD1 mice (P1-P2), the latter for in vitro cell culture, were purchased from Charles River (Montreal, Canada). For lysolecithin demyelination, the NG2^{CreER}:MAPT^{mGFP} mice at 8–10 weeks were injected intraperitonially with 2 mg tamoxifen (100 µL of 20 mg/mL tamoxifen in corn oil) (Sigma) daily for 3 consecutive days to induce recombination. Demyelination was then induced in mice at least 5 days after the last tamoxifen injection to allow tamoxifen to be washed out. Genotyping was conducted using protocol provided online through Jackson Laboratories.

Plasmid construction

pJEP317-pAAV-U6SaCas9gNRA (SapI)-EFS-GFP-KASH-pA, pJEP312-pAAV-CMV-SaCas9-P2A-HAFLAGHA-KASH-pA (gifts from Jonathan Ploski[1] (Addgene plasmid # 113694); (Addgene plasmid # 113689)), and pAAV-GFP-eGFP (gift from Bryan Roth (Addgene plasmid # 50473)) were obtained from addgene. The AAV vectors were modified to drive expression of GFP and SaCas9 specifically in astrocytes. The EFS promoter of pJEP317-pAAV-U6SaCas9gNRA (SapI)-EFS-GFP-KASH-pA was excised by AgeI and Xba restriction enzyme digestion and replaced with the GFAP promoter sequence PCR amplified from pAAV-GFAP-GFP to generate pAAV-U6-GFAP-GFP-KASH-pA using the NEBuilder hifi DNA assembly cloning kit (New England Biolabs). Likewise, the CMV promoter of pJEP312-pAAV-CMV-SaCas9-P2A-HAFLAGHA-KASH-pA was excised by digestion with XbaI and AgeI and replaced with the GFAP promoter sequence PCR amplified from pAAV-GFAP-GFP to generate pAAV-GFP-SaCas9-P2A-HAFLAGHA-KASH-pA.

Potential single guide RNAs (sgRNAs) with the SaCas9 PAM sequence (NNGRR) targeting the mouse fibulin-2 gene were designed using the Broad Institute GPP sgRNA designer[2,3] using the cDNA sequence of Flbn2 (accession NM_007992). The top ranked sgRNA (5'-ACCCTCCTGCATGACACTTCG-3'), targeting the antisense strand of exon 2 was chosen. Complementary oligonucleotides with appropriate overhang sequences and 5' phosphorylation modifications 5'-P-ACCGACCCTCCTGCATGACACTTCG-3'and 5'-P-AACCGAAGTGTCATGCAGGAGGGTC-3' were annealed and subcloned into BspQI-digested pAAV-U6-GFAP-GFP-KASH-pA to generate pAAV-U6FblnsgRNA-GFP-KASH-pA. For the non-target control, sgRNA targeting a lacZ sequence[4] (GTGCGAATACGCCCACGCGAT) was used by subcloning the oligos 5'-P-ACCGTGCGAATACGCCCACGCGAT-3' and 5'-P-AACATCGCGTGGGCGTATTCGCAC-3' into the BspQI site of pAAV-U6-GFAP-GFP-KASH-pA to generate pAAV-U6lacZsgRNA-GFAP-GFP-KASH-pA. All plasmid constructs were verified by restriction enzyme mapping and Sanger DNA sequencing.

AAV production

AAV viral vectors containing the PHP.eB capsid were generated using the methods of Challis et. al.[5] PHP.eB capsid has been engineered to efficiently transduce the central nervous system[6]. Briefly, 293FT cells (Thermofisher) were grown to ~90% confluency in Corning hyperflasks (Corning) and co-transfected with 129 µg pHELPER (Agilent), 238 µg rep-cap plasmid encoding RH10 (a gift from James M. Wilson (Addgene plasmid # 112866) and 64.6 µg of transfer plasmid using the PEIpro transfection reagent (Polyplus). AAVs were precipitated from media harvested after 3 days and 5 days using 40%PEG/2.5M NaCl in buffer containing 500 mM NaCl, 40 mM Tris Base and 10 mM

548 $MgCl_2$. The lysate was incubated with 100 U/mL salt-active nuclease (Arcticzymes) at
549 37^{O}C for 1 h and then centrifuged at 2000 xg for 15 min. AAV was purified from the
550 resulting lysate using an iodixanol step gradient containing 15, 25, 40 and 60% iodixanol
551 in optiseal tubes (Beckman) followed by centrifugation at 350,000 xg using a Type 70 Ti
552 ultracentrifuge rotor (Beckman). Following centrifugation, the AAVs were harvested from
553 the 40% layer using a 10 ml syringe and 16-guage needle, diluted in 1XPBS containing
554 0.001% pluronic F68 (Gibco) and filtered using a 0.2 um syringe filter. The AAVs were
555 concentrated and buffer-exchanged by 5 rounds of centrifugation using Amicon Ultra-15
556 100 kDa molecular weight cut off centrifugal filter units (Millipore). The titer was
557 determined using the qPCR Adeno-Associated Virus Titration kit (Applied Biological
558 Materials) and the purity was verified by SDS-PAGE and total protein staining using
559 instant blue reagent (Expedeon).

560 The indicated pairs of vectors encoding Cas9 under the control of a GFAP
561 promoter and gRNA (FBLN2 specific or non-target control) were co-delivered by retro-
562 orbital injection to 6- to 8-week-old WT C57BL/6J mice at 3×10^{11} vg/virus 2 weeks before
563 EAE induction or lysolecithin surgery.

564 **Experimental autoimmune encephalomyelitis (EAE) induction.**

565 Littermate female wildtype, heterozygous (Fbln2+/-) and homozygous (Fbln2-/-) mice
566 (10–12 weeks old) were injected subcutaneously with 50 µg MOG35-55 peptide
567 (synthesized by Protein and Nucleic acid facility, Stanford University) emulsified in
568 complete Freund's adjuvant (CFA) (Thermo Fisher Scientific) supplemented with
569 10 mg/ml heat-inactivated Mycobacterium tuberculosis H37Ra (Sigma-Aldrich). A total of
570 100 µl emulsion was injected at two sites into hind flanks. Pertussis toxin (300 ng per

200 µl; 180, List Biological Laboratories) was intraperitoneally injected on days 0 and 48 h after MOG immunization. Clinical signs of EAE were monitored daily on a scale of 0–15 [7]. For the tail, score of 0,1 and 2 represent no signs, half-paralyzed tail and a fully paralyzed tail, respectively. For each of the hind- or forelimbs, 0 signifies no signs, a score of 1 is given to a mouse with a weak or altered gait, a score of 2 reflects paresis, and a score of 3 is given to a fully paralyzed limb. Mortality corresponds to a score of 15. Mice were euthanized with ketamine (100 mg/kg) and xylazine (10 mg/kg) injected intraperitoneally and then perfused with PBS through the left ventricle of the heart. Following PBS perfusion, lumbar and thoracic spinal cord were dissected for RNA/protein extraction and immunohistochemistry, respectively. For RNA/protein extraction, spinal cords were immediately flash frozen in liquid nitrogen and stored at -80 °C.

Lysolecithin-induced demyelination

Lysolecithin was injected into the ventral spinal cord to induce experimental demyelination as described previously[8]. Mice were first anesthetized with ketamine and xylazine (100 mg/kg and 10 mg/kg, respectively) injected intraperitoneally. The analgesic buprenorphine (0.05 mg/kg) was administered subcutaneously prior to surgery and 12 h post-surgery. To induce focal demyelination in the ventrolateral white matter of the spinal cord, 1% lysolecithin (Sigma L1381) resuspended in 0.5 µl sterile phosphate buffered saline (PBS) was injected at a rate of 0.25 µl/min over 2 min. A 10 µl Hamilton 34-gauge needle was inserted 1.3mm into the ventral spinal cord between the T3 and T4 vertebra. Mice were then sutured and monitored until recovery. Mice were euthanized at 7,14-, and 21-days post-injection of lysolecithin with a lethal dose of ketamine/xylazine. Animals

were then perfused with 15 mL of PBS. The lower cervical and upper thoracic section of the spinal cord was dissected.

Collagenase-induced ICH

The procedure for collagenase-induced ICH in mice is described in a previous study [9]. Briefly, mice were first anesthetized with ketamine (100 mg/kg) and xylazine (10 mg/kg). A 0.5 mm cranial burr hole was made with a microdrill in the skull above the right striatum according to the following coordinates (2.0 mm lateral and 0.8 mm anterior to the bregma). Collagenase type VII (0.05 U) dissolved in 0.5 µL of saline was injected through the hole until 3.2 mm beneath the skull, ending in the right striatum. The injection (5min) was controlled by a UMP3 UltraMicroPump. The needle was kept inside the brain for another 5 min to prevent reflux before removal. Finally, the surgical site was sutured and disinfected.

Immunofluorescence staining

Spinal cords were post-fixed overnight in 4% PFA at 4 °C, then dehydrated in 30% sucrose solution for 72 h. Tissues were then frozen in FSC 22 Frozen Section Media (Leica) and cut coronally or longitudinally into 20 µm sections using a cryostat (ThermoFisher Scientific). Tissues were collected on to Superfrost Plus microscope slides (VWR) and stored at -20 °C prior to staining.

Slides were thawed at room temperature for 15 min, then fixed with 4%PFA for 15 min. Tissue sections were permeabilized with 0.25% Triton X-100 in PBS 10 min for intracellular markers. Blocking of samples was performed using horse serum blocking solution (0.01M PBS, 10% horse serum, 1% bovine serum albumin (BSA), 0.1% cold fish skin gelatin, 0.1% Triton-X100, and 0.05% Tween-20) for 1 h at room temperature.

Tissues were then incubated overnight at 4°C with diluted primary antibodies in antibody dilution buffer (PBS, 1% BSA, 0.1% cold fish stain gelation, and 0.1% Triton X-100). Next, slides were washed three times, 5 min each with PBS containing 0.1% Tween-20 and then incubated with the corresponding fluorophore-conjugated secondary antibodies (1:400; Jackson ImmunoResearch Laboratories) and 4′,6-diamidino-2-phenylindole (DAPI) (1 µg/ml, Sigma) suspended in the antibody dilution buffer for 1 h at room temperature. After washing (3x, 5 min each), slides were mounted using Fluoromount G (Southern Biotech). Isotype controls and secondary antibody controls were included.

Human paraffin sections were cut (7 µm) using a Leica RM2135 Microtome. After deparaffinization, sections were subjected to antigen retrieval by boiling in 10 mM sodium citrate buffer (pH 6.0) for 20 minutes, then they were incubated with 4% horse serum to block nonspecific binding and incubated with primary antibodies overnight at 4°C. Secondary antibodies were then added for 60 minutes.

For MBP staining, sections were delipidated before fixation by sequential wash with 50%,70%, 90%, 95%, 100%, 95%, 90%, 70%, and 50% ethanol.

The following primary antibodies were used for immunofluorescence microscopy to identify specific targets: rabbit anti-mouse myelin basic protein (MBP)(1:200; Abcam), rabbit anti-mouse/human Olig2 (1:200, Millipore), goat anti-mouse platelet-derived growth factor receptor α(PDGFRα) (1:200, R&D Systems), mouse anti-mouse adenomatous polyposis coli (APC) (1:200, Millipore, clone CC-1), chicken anti-GFP (1:500, Aveslab), rabbit anti-ionized calcium-binding adaptor molecule1 (Iba1) (1:500, Wako), rat anti-mouse CD45 (1:50, Pharmingen), rat anti-human CD45 (1:500, Invitrogen, MA5-17687), rabbit anti-mouse NF-H (1:1,000; Encor Biotechnology), goat anti-mouse/human GFAP

(1:1000, Novus), rat anti-HA tag (1:500, Novus), rat anti-mouse CD68 (1:500; BioLegend), rabbit anti-mouse cleaved caspase-9 (1:200; Invitrogen), rabbit anti-mouse Hes5 (1:200, Abcam), rabbit anti-mouse/human fibulin-2 (1;100, Invitrogen, cat#PA5-75510, Immonogen: Synthetic peptide corresponding to amino acids 289-334 of Human Fibulin2) and rabbit anti-mouse/human fibulin-2 (1;100, Invitrogen, cat# PA5-79239, Immonogen: A synthetic peptide corresponding to amino acids 188-205aa at the N-terminus of human Fibulin2.

Images were captured on the Leica TCS SP8 confocal laser scanning microscope and Olympus VS110 Slide scanner. The z-stacks of confocal images were analyzed with ImageJ (NIH). IMARIS software (Bitplane) was used for 3D rendering of confocal image z-stacks. The lesion region of interest (ROI) was determined by loss of MBP staining or as a hypercellular area. A similar field used for normal appearing white matter (NAWM).

Spinal cord cell isolation for scRNA-seq

EAE mice from WT, Fbln2+/- and Fbln2-/- (3 mice in each group) were euthanized with a lethal dose of ketamine and xylazine 18 days after EAE induction, and then perfused via cardiac puncture with 15 ml of HBSS (without Ca2+, Mg2, ThermoFisher Scientific) containing 1 μM flavoperidol (Sigma) and 5 μg/ml actinomycin D (Sigma). Spinal cords were isolated and kept in 1ml of dissection buffer containing (HBSS (without Ca2+, Mg2+),1 μM flavoperidol, 5 μg /ml actinomycin D, and 27.1 μg /ml anisomycin (Sigma). Thoracic and lumbar parts of spinal cords were cut into pieces. The single cell suspension was prepared using Neural Tissue Dissociation kit (Miltenyi Biotec) and gentleMACS Dissociator with Heaters (Miltenyi Biotec) according to the manufacturer's instructions. Transcription and translation inhibitors (1 μM flavoperidol, 5 μg/ml actinomycin D and 27.1 μg/ml anisomycin) were added to enzyme mix. Myelin debris was removed from the

663 cell suspension using Debris Removal solution (Miltenyi Biotec). Cells were then
664 resuspended in PBS containing 1% heat-inactivated fetal bovine serum (Sigma).

665 **ScRNA library preparation**

666 Once a single-cell suspension was generated as described above, scRNA-seq was
667 performed using the 10x Genomics platform with Chromium Next GEM single cell 3′
668 reagent kits v3.1. An appropriate volume of cells, as determined from the user guide for
669 recovery of 4,000 cells, was loaded on the Chromium single-cell controller chip. The
670 Chromium Next GEM Single Cell 3′ v3.1 library and gel bead kit were used to prepare
671 scRNA-seq libraries. Post cDNA amplification QC and quantification, as well as library
672 construction QC, were done using an Agilent Bioanalyzer high-sensitivity DNA chip for
673 use with the Agilent 4200 TapeStation System. For sequencing, all 9 libraries were pooled
674 and loaded at 300 pM on a Illumina NovaSeq 6000 sequencing system using a S1
675 flowcell. A 28-bp read 1 was used to sequence the cell barcode and UMI.
676 10-bp i5 and i7 index reads were used to sequence the sample index and a 90-bp read 2
677 was used to sequence the transcript using paired-end, dual index sequencing.

678 **ScRNA-seq analysis**

679 The base call files were processed using 10x Genomics Cell Ranger v6.1 pipeline with
680 reads aligned to the mm10 mouse reference transcriptome. The cellranger aggregate
681 pipeline was run to generate an expression matrix with the nine combined libraries, with
682 the normalization setting set to “None”. The sequencing depth obtained ranged from
683 38,700 - 48,959 reads/cell. The generated expression matrix was then analyzed using
684 the package Seurat v.3 in R v4.2.3 [10]. The expression matrix comprised 36,251 cells. The
685 data were filtered for the following parameters: cells with >200 and < 7500 genes and

686 percentage of mitochondrial genes <10%. Post filtering, the expression matrix contained
687 34,395 cells. Data from all 9 libraries were then integrated and normalized with the
688 SCTransform function in Seurat using all 23312 features, 3000 variable features. Cell
689 recovery from all 3 groups was comparable (WT:12606; Het:11073; Homo:10716 cells).
690 A PCA reduction was performed, and 30 significant PCA dimensions were taken into
691 account. Clusters were determined using FindNeighbours and FindClusters function,
692 which was performed with a resolution of 0.3. Unsupervised integrated alignment of all
693 cells from the 9 spinal cords of EAE mice (3 mice per group delineated 17 clusters which
694 were present in all experimental groups (Fig. 2e). Cluster annotation was manually done
695 based on the expression of lineage-specific hallmark genes. Using lineage cell markers;
696 clusters 0 was identified as border associated macrophage (BAM) based on various
697 markers (*Arg1, Lyz2, Ms4a7, Lgals3, Fabp5*); cluster 1 and 6 were identified as
698 homeostatic microglia (MG) (*Cx3cr1, Tmem119, P2ry12, Siglech*); cluster 2 as activated
699 microglia (*C1qa, Cst3, Trem2, Ctsz, Hexb);* cluster 3 as T cell (*Skap1, Cd3g, Trbc2, Cd4,*
700 *Cd8a*); cluster 4 and 12 as oligodendrocyte lineage cell (*Plp1, Ptgds, Nkain2, Apod, Olig1,*
701 *Mbp, Mog*); cluster 5 as activated peripheral monocyte/macrophages (Mon/MAC) *(Ccr2,*
702 *Msr1, Mrc1, Ms4a7, Ly6c*); cluster 7 as dendritic cell (DC) (*H2-Ab1, H2-Aa, Cd74, Napsa,*
703 *Ciita, Alcam*); cluster 8 as NK/NK T cell (*Gzma, Klre1, Nkg7, Cd8a, Cd3e, Skap1,Trbc2*);
704 cluster 9 as neutrophils (*Ly6g, Retnlg*); cluster 10 as B cells (*Igkc, Cd79b, Cd19, Ighm*);
705 cluster 11 as proliferating cells (*His1h1b, Top2a, Birc5, Pclaf*); cluster 13 as fibroblast
706 (*Mgp, Sparcl1, Col1a2, Pdgfrb, Aqp4, Slc4a4, Igfbp7*); and cluster 14 as astrocytes (*Nnat,*
707 *Ecrg4, Mt3, Aqp4, Gfap, Sparcl1, Slc1a2*) (Fig. 2d,e, Extended Data Fig. 3a, b and Supp
708 Table 1). Oligodendrocyte lineage cells (2592 cells) were subset and re-clustered into 7

709 distinct subcluster determined by 10 principal components and 0.4 clustering resolution
710 (Extended Data Fig. 3b, d and Supp Table 3). Differentially upregulated genes (DEGs)
711 were determined through the FindMarkers functions. DEGs with a statistically significant
712 P value less than 0.05 were included for analysis.

713 **Sequencing and analysis of total RNA for OPCs treated with or without FBLN2**

714 Three × 10^5 OPCs were grown on FBLN2 (10 μg/ml) or PBS (control) coated wells for 6
715 hours in differentiation medium (3 wells per condition). RNA was isolated from cells using
716 the RNeasy Kit (Qiagen) with DNA removal and according to the manufacturer's
717 instructions. Quality and quantity of the isolated RNA was determined by TapeStation and
718 Fragment Analyzer (Agilent Technologies). RNA was subjected to enrichment of
719 polyadenylated [poly(A)] mRNA, cDNA synthesis, and then prepared into libraries using
720 NEBNext Ultra II Directional RNA Library Prep Kit (New England Biolabs). Libraries were
721 then sequenced using a NextSeq 500 system (Illumina) using a single NextSeq 75 cycle
722 high output run. FastQC (v0.11.5) was used to determine the quality of sequencing reads
723 and cutAdapt (v1.13) was used for quality trimming (q20). Kallisto (v0.43.1) was used for
724 quantifying abundances of transcripts. Kallisto index was built with reference
725 transcriptome GRCm39. The R package tximport was used to summarize transcript level
726 abundances from kallisto to gene level. The R package "DESeq2" was used for
727 differential expression analysis. DEGs with adjusted p-value < 0.05 were considered
728 statistically significantly and included for analysis.

729 **Ingenuity pathway analysis**

730 DEGs from scRNA-seq or bulk RNA-seq experiments were analyzed using the Ingenuity
731 Pathway Analysis (IPA) software(QIAGEN Inc.,

https://www.qiagenbioinformatics.com/products/ingenuitypathway-analysis). The Core Expression Analysis based on the average log fold-change ratios was performed, where both direct and indirect relationships and interaction and causal networks filtered by experimentally observed confidence were predicted.

Protein isolation and measuring protein concentration

Protein from spinal cord tissues or cell culture were isolated using ice-cold radio immunoprecipitation assay (RIPA) lysis and extraction buffer (Thermo Scientific) containing protease and phosphatase inhibitors (Cell Signaling Technology). Astrocyte medium was removed, and cells left behind in each well of a 6-well plate (1 million cell) were lysed in 500µl of cold RIPA buffer. After 5 min, lysate was collected using cell scraper and then centrifuged at 15000 rpm for 15 min at 4°C. The supernatant containing protein was kept at -80°C. Proteins were quantified using the bicinchoninic acid (BCA) assay relative to a bovine serum albumin (BSA) standard. BCA mix was prepared accordingly: 190 µl of BCA (Sigma) was mixed with 10 µl of copper sulfate (Sigma). 200 µl of BCA mix was added to each well of 96-well plate containing 25 µl of diluted sample in water. Serial dilution of BSA solution (2 mg/ml in water) was prepared as standard control. Samples were incubated for 10-15 min at 37°C. The absorbance at 560 nm was measured using the SpectraMax Plus 384 Microplate and the protein concentration was calculated according to standard curve.

Western Blot

The proteins were loaded into sodium dodecyl sulphate (SDS) gels (NuPAGE 4-12% Bis-Tris Gel, Invitrogen) and ran with HiMark™ Pre-stained Protein Standard (Invitrogen) at 250V for 40 min. Then, the proteins were transferred using electroblotting to an 0.2 µm

polyvinylidene fluoride membrane (PVDF) (GE Healthcare Life Science). The PVDF membrane was rinsed with tris-buffered saline (TBS) containing 0.05% Tween 20 (TBST) and blocked with 10% m/v skim powdered milk in TBS for 1h at room temperature. Primary antibodies for rabbit anti-mouse cleaved caspase-9 (1:500; Invitrogen), rabbit anti-mouse Hes5 (1:500, Abcam), rabbit anti-mouse/human fibulin-2 (1;200, Invitrogen, cat#PA5-75510 and PA5-79239) were added to 3% milk in TBS and incubated overnight at 4°C. The membrane was washed five times (5-min/each) with TBST followed by incubation with secondary antibodies conjugated with horseradish peroxidase (HRP) for 1h at room temperature. The membrane was washed five times (5 min each) with TBST before visualization using enhanced chemiluminescent (ECL) substrate (SuperSignal™ West Femto Maximum Sensitivity Substrate, Thermo Scientific) and imaging with the BioRad ChemiDoc system. To probe for β-actin, the membranes were washed using Restore™ Western blot stripping buffer (Thermo Scientific) for 30 min before blocking with 5% m/v BSA in TBS for 1h at room temperature. The membrane was then incubated with primary antibody HRP anti-beta actin antibody (Abcam) in 3% m/v BSA in TBS for 1h at room temperature before washing (5x/ 5min each). The blots were visualized and imaged using the same methods as above. The Western Blots were quantified using the gel analyzer function in ImageJ. The relative amount of protein was normalized to the actin bands and compared to the control bands.

RNA isolation, cDNA synthesis, and real-time PCR

Total RNA was purified from cells or lumbar spinal cords using RNeasy Mini kit (Qiagen) according to the manufacturer's instructions and stored at −80 °C. The concentration and quality of RNA were determined by measuring absorbance at 260/280 nm using a

778 nanodrop spectrophotometer (Thermo Fisher Scientific). To reduce DNA contamination,
779 samples were treated by DNase (Ribonuclease-Free DNase Set ,QIAGEN). RNA was
780 reverse-transcribed to cDNA with 1 µg total RNA using miScript II RT Kit (Qiagen) for
781 mRNA expression analyses according to the manufacturer's instructions. Transcripts
782 were quantified by Real time PCR RT-qPCR on the QuantStudio 6 Flex Real-Time PCR
783 System (Thermo Fisher Scientific) using QuantiFast SYBR Green master mix (Qiagen)
784 and Quantitect Primers: Actb (Qiagen, QT00095242), Gapdh (Qiagen,QT01658962),
785 (Fbln2_2272567 ,SBM1028417), (Notch1, QT00156982), (Bcl2, QT00156282) and
786 (Bax1, QT00102536) with the following cycling conditions: 95 °C for 5 min, 40 cycles of
787 denaturation at 95 °C for 30 s, annealing at 60 °C for 30 s and extension at 72 °C for 30
788 s. The relative expression levels were analyzed by 2-ΔΔct method, with expression levels
789 normalized to β-actin and glyceraldehyde-3-phosphate dehydrogenase (Gapdh)
790 housekeeping genes.

791 **Cell Culture:**

792 *Mouse oligodendrocyte progenitor cells (OPC)* of over 80% purity were prepared from
793 postnatal brains as previously described [11]. Cortices from postnatal day P0-2 mouse pups
794 were isolated using a dissection microscope and dissociated with a digestion cocktail
795 containing papain (1.54 mg/ml, Worthington), DNase (60 µg/ml, Sigma), and L-cysteine
796 (360 µg/ml, Sigma) in a 37 °C water bath for 30 min. Cell suspension was centrifuged at
797 300xg for 10 min. Cell pellet were resuspended in DMEM (Gibco) containing10% FBS,
798 1% GlutaMAX, 1% sodium pyruvate, and 1% Penicillin-Streptomycin (all from Gibco) and
799 plated in T-75 culture flasks pre-coated with poly-L-lysine (100 µg/mL, Sigma). The mixed
800 glial culture was incubated at 37 °C, 8.5% CO2 for 9 days with medium change after 4 h,

on day 3, 6 and 9. On day 9, flasks were shaken on an orbital shaker at 220 rpm for 12-16 h to isolate OPCs and microglia from astrocytes. To remove microglia, the supernatant were added to a 100 mm tissue culture dish and were incubated for 30 min. Non-attached cells (OPCs) were harvested and centrifuged at 300xg for 10 min. Cells were then plated at a density of 1×10^4 cells per well in 96-well flat bottom black/clear plates pre-coated with poly-L-lysine in oligodendrocyte differentiation or proliferation medium and incubated at 37 °C and 8.5% CO2 for indicated time points. Oligodendrocyte differentiation medium comprised DMEM containing 2% (v/v) B27 supplement (Gibco), 1% (v/v) oligodendrocyte supplement cocktail (described below), 1% (v/v) GlutaMAX™ (Gibco), 100 µM sodium pyruvate (Gibco), 1% (v/v) Penicillin-Streptomycin (Gibco), 50 µg/mL holo-transferrin (Sigma), 5 µg/mL N-acetyl-L-cysteine (Sigma), 5 µg/mL insulin (Sigma), 50 ng/mL ciliary neurotrophic factor (CNTF) (PeProTech),10 µg/ml Biotin (Sigma) and 0.01% (v/v) Trace Elements B (Fisher Scientific) . Oligodendrocyte supplement cocktail contained 100 mL DMEM with 1% BSA, 0.6 mg progesterone (Sigma), 161 mg putrescine (Sigma), 0.05 mg sodium selenite (Sigma), 4 mg 3,3′,5-triiodo-L-thyronine (Sigma) and 4mg L-thyroxine (Sigma). Oligodendrocyte proliferation medium comprised DMEM containing 2% (v/v) B27 supplement (Gibco), 1% (v/v) GlutaMAX™ (Gibco), 100 µM sodium pyruvate (Gibco), 1% (v/v) Penicillin-Streptomycin (Gibco), 5 µg/mL insulin (Sigma), 10 ng/ml FGF factor (PeProTech) and 10 ng/mL PDGF and FGF factor (PeProTech).

Plates were coated with recombinant protein or PBS for 3 h at 37 °C; FBLN2 (1, 5 and 10 µg/ml; R&D), FBLN1(10 µg/ml; R&D), FBLN3 (10 µg/ml; R&D), Jagged1 (2 µg/ml; R&D) diluted in PBS. Jagged1 was used as a positive control for Notch signaling (Extended Data Fig. 6i-k). To hinder signaling pathways, OPCs were pretreated for 30 min with

different inhibitors including Notch signaling (SAHM1, 10 uM), ROCK (Y27632, 1 μM), MEK/ERK (PD98059, 10 μM), P38MAPK (SB202190, 10 μM), PI3-K/AKT/mTOR (urolithin, 10 μM), Wnt/β-catenin (endo-IWR1,1 μM), Src/Syk (MNS,10 μM), BMP4 (LDN193189,100 nM) or Smad3 (SIS3, 10 μM) inhibitor as well as 50 μg/ml blocking antibodies against mouse integrin-beta3 (CD61, Invitrogen), mouse integrin-beta1 (CD29, Invitrogen) or mouse integrin-beta6 (Millipore). All inhibitors were purchased from Tocris.

Mouse primary astrocyte, *microglia and neurons culture*: Astrocytes were obtained from a mixed glial culture (OPC culture). When the flasks were shaken on day 9 to remove microglia and oligodendrocytes, the astrocyte monolayer that remained was cultured in DMEM supplemented with 10% heat-inactivated FBS, 1% GlutaMAX, 1% sodium pyruvate, and 1% Penicillin-Streptomycin. These cells were passaged twice and cultured with decreasing concentrations of FBS (3% and 1%). Prior to treatment with cytokines, astrocytes were seeded in 6-well plates at 1 x 10^6 cells/mL in DMEM with 1% FBS overnight. Cells were treated with 10 ng/mL of cytokines, including tumour necrosis factor-α (TNF-α), interleukin-1β (IL-1β), interferon-γ (IFN-γ), and transforming growth factor-β (TGF-β).

Mouse microglia of over 90% purity were prepared from neonatal brains as previously described [12]. Non-adherent fraction collected from neonatal mixed glia cultures were plated in poly-L-ornithine-coated 96-well flat-bottom black/clear plates at 5 × 10^4 cells per well. Cells were incubated in Neurobasal Plus medium (Gibco).

Primary mouse cortical neurons were obtained from embryonic day 15–16 pups. Neurons were isolated and grown in Neurobasal Plus medium (Gibco) supplemented with B27

Plus supplement (Gibco) as previously detailed [12]. 0.75–1 × 10^5 neurons were seeded in each well of the poly-L-ornithine-coated 96-well flat-bottom black/clear plates.

Bone marrow derived macrophages (BMDMs) were prepared from femurs and tibiae of C57/BL6 mice. Cells were cultured in DMEM containing 10% FBS, 1% penicillin-streptomycin (Gibco), 1% sodium pyruvate (Gibco), 1% GlutaMAX™ (Gibco), and 10% L929 conditioned media at 37°C, 8.5% CO2 in uncoated 100 mm plastic for 8–10 days. Media was changed on day 5 and 7. BMDMs were dissociated from dishes using cell scrapers and then seeded in 96-well plates at a density of 5 × 10^4 cells per well in same media without L929 conditioned media. Plates were incubated at 37 °C in 5% CO2. After 24 h, the media was changed to serum-free DMEM, and cells were treated with LPS (100 ng/ml) for 24 h. Conditioned medium was collected from microglia and BMDM culture to measure levels of TNF-α using ELISA kit (Invitrogen), which was performed according to manufacturer's instructions.

Human OPCs: Human brain tissues were obtained from patients undergoing surgical resection to treat intractable epilepsy. The use of the surgical material for the current study was approved by The Conjoint Health Research Ethics Board at the University of Calgary. After centrifuge in 30% percoll for 30 min at 15,000 rpm. the cell layer was collected and resuspended in MEM medium (Gibco) supplemented with 5% FCS. Cells were incubated for 48 h at 37 °C in a 5% CO2 environment. Then, the medium containing floating cells (enriched OPC) was collected and plated on poly-L-ornithine-coated 96-well flatbottom black/clear plates at a density of 5 × 10^4 cells per well for 24 h in DMEM/F12 containing 1% (v/v) N2 supplement (Gibco), 0.1% (v/v) 3,3′,5-triiodo-L-thyronine (Sigma), 10 nM biotin (Sigma), 100 µg ml/ml BSA (Sigma), 10 ng/ml PDGF (PeproTech), 1% (v/v)

GlutaMAX (Gibco), 100 μM sodium pyruvate (Gibco) and 1% (v/v) penicillin–streptomycin (Gibco). After 24 h of cell attachment, the culture medium was changed to the same medium without PDGF.

Human Neurons: Human fetal brain tissues from legal abortions were used to culture neurons. The use of the fetal samples is approved by The Conjoint Health Research Ethics Board at the University of Calgary. As described previously [12], 0.75–1 × 105 neurons were seeded into each well of poly-L-ornithine-coated 96-well flat-bottom black/clear plates in 100 μl of AIM V media (Gibco). Purity of culture was over 80%. After 24–48 h of culture, cells were used for experiments.

Immunofluorescence staining of cells

Cells were fixed for 15 min at room temperature using 4% paraformaldehyde, rinsed with PBS and then permeabilized with 0.1% Triton X-100 for 10 min at RT. Odyssey Blocking Buffer (LI-COR) was used for blocking step for 1h at room temperature. Primary antibodies were diluted in blocking buffer and added to cells. Cells were incubated with primary antibodies including mouse anti-mouse/human sulfatide O4 (oligodendrocyte lineage cell marker) (1:50, R&D), rabbit anti-mouse MBP (1:200, Abcam), rabbit anti-mouse/human Olig2 (1:200, Millipore), mouse anti-human MAG (1:100; Abcam), rabbit anti-mouse/human Iba1 (1:500, Wako), goat anit-mouse/human GFAP (1:1000, Novus), mouse anti-human/mouse tubulin-β3 (1:500, BioLegend, Clone Tuj1), rabbit anti-mouse cleaved caspase-3 (1:500, Cell Signaling), chicken anti-GFP (1:500, Aveslab) and rat anti-HA tag (1:500, Novus) overnight at 4 °C, then washed 3× (5 min each) with PBS. Cells were subsequently incubated with corresponding fluorophore-conjugated secondary antibodies (1:400 Jackson ImmunoResearch Laboratories) and DAPI (1 μg/ml,

Sigma) at room temperature for 1h and washed 3× (5 min each) with PBS. Cells were then imaged using ImageXpress (Molecular Devices).

ImageXpress acquisition and MetaXpress analysis

Labeled cells in 96-well flat bottom black/clear plates were imaged with ImageXpress Micro XLS High-Content Analysis System (Molecular Devices). For each well, twelve images (field of views; FOVs) were acquired for quantitative analysis by the MetaXpress High-Content Image Acquisition and Analysis software (Molecular Devices). “Neurite outgrowth” and “Multiwavelength cell scoring” modules were used to measure OPC process outgrowth, cell survival and cell number for a particular marker. Data from the 12 images were averaged to a single data point per well and then normalized to control wells for each experiment.

OPC proliferation analysis

OPCs were cultured in proliferation media (supplemented with growth factors PDGFRα (10 ng/ml) and FGF (10 ng/ml) overnight. Cells were then treated with 5-ethynyl-2'-deoxyuridine (EdU, 10 µM) for 6h before detection of incorporated EdU by Click-iT EdU proliferation assay. Following fixation and cell permeabilization, EdU staining was conducted according to the manufacturer's instructions using the Click-iT Plus EdU alexa flour 647 imaging kit (Thermo Fisher Scientific). ImageXpress Micro XLS High-Content Analysis System was used for analysis of cells.

Live cell imaging of OPCs

Mouse OPCs were plated at 1×10^4 cells per well in 100 µL of differentiation medium into a 96-well flat bottom plate coated with or without FBLN2 (10 µg/mL) in the presence of propidium iodide (Thermofisher Scientific,1 µg/mL). The cell survival and process

outgrowth were monitored using a real-time cell imaging system (IncuCyte live-cell ESSEN BioScience Inc). Images of the cells were taken for a total of 48 hours at 30 min intervals.

Cell cycle analysis

Mouse OPCs plated at 1×10^5 cells per well in 24-well flat bottom coated plates with PBS (control) or FBLN2 (10 µg/mL). Cells were incubated in differentiation medium for 12 hours, and then detached with accutase (STEMCELL) and fixed with PFA 4%. Cells were stained with FxCycle PI/RNase staining solution (Thermofisher Scientific) and subjected to flow cytometry analysis. Attune NxT flow cytometry was used for analysis of cells (Thermo Fisher Scientific). FlowJo version 10.7.2 was used to analyse the data (Treestar).

T cell proliferation analysis

Naïve $CD3^+$ T Cells were isolated from single-cell suspensions of splenocytes (6 to 8-week-old C57BL/6 mice) using the EasySep Kit (STEMCELL) by negative selection. Purified cells were seeded in 24-well plates at a density of 1×10^6 cells in 1 ml of RPMI 1640 medium (Gibco) supplemented with 10% FBS (Gibco),1% GlutaMAX, 1% sodium pyruvate, and 1% Penicillin-Streptomycin (100 mg/ml) (Gibco). Cells were labeled with 1 µM of carboxyfluorescein succinimidyl ester (CFSE) dye (Thermo Fisher Scientific), and FBLN2 was then added to the test group. Cells were stimulated with anti-CD3 (0.5 µg/ml) and anti-CD28 (0.2 µg/ml) antibodies (eBioscience). After 72 h, cells were analyzed using flow cytometry (FACS Attune NXT) to measure CFSE dilution, where a more proliferative culture would have more cycles of diluted CFSE. FlowJo version 10.7.2 was used to analyse the data (Treestar).

939 **Transfection of primary mouse OPC**

940 Freshly isolated OPCs were electroporated using the 4D-nucleofector device (Lonza) and
941 P3 Primary Cell 4D-Nucleofector Kit (Lonza) according to the manufacturer's instruction
942 in 20-µL-format Nucleocuvette strips. Cells were transfected with two *Notch1* siRNA (200
943 nM/each, Invitrogen) or negative control siRNA (200nM, Invitrogen) and 0.4 µg pmaxGF
944 Vector using P3 Primary Cell Nucleofector Solution and program CL-133. Post
945 Nucleofection, cells were cultured in differentiation medium at 25×10^3 cells per well in
946 96-well flat bottom/black plate coated with FBLN2 (10 µg/mL) or PBS (control). After 24
947 hours, cells were fixed, stained for O4 marker and then analyzed using ImageXpress
948 Micro XLS High-Content Analysis System. Transfection efficiency was between 45–60
949 % (Extended Data Fig. 6l).

950 **NOTCH1 expressing HEK293 cell line**

951 Stable NOTCH1 expressing HEK293 cell line was generated using piggyback
952 transposase system. The full-length sequence of *Notch1* was excised from pCS2 Notch1
953 Full Length-6MT (Addgene plasmid # 41728). Notch1 sequence was subcloned into the
954 PB-CMV-MCS-EF1α-Puro piggybac expression vector (System Biosciences) using the 5'
955 EcoRI and 3' BamHI restriction sites. The sequences of all constructs were verified by
956 Sanger DNA sequencing. Next, HEK293 cells were transfected with 500 ng of the
957 construct and 200 ng of transposase using Lipofectamine 2000 (Invitrogen). Drug
958 selection (puromycin 1ug/ml) started on day 3 and was continued for 2 to 3 weeks.

959 **Dual luciferase reporter assay**

960 The dual luciferase assay was carried out according to the instruction of Notch Pathway
961 Reporter kit (BPS Bioscience). Briefly, NOTCH-expressing HEK293 cells (3×10^4 per

well) were transfected with 1 µL CSL (CBF1/RBP-Jκ) luciferase reporter vector and constitutively expressing Renilla luciferase vector (positive control) using Lipofectamine 2000 (Invitrogen). Luciferase reporter vector contains the Firefly luciferase gene under control of multimerized CSL responsive element. Activity of Notch signaling results in proteolytic cleavage of the NOTCH receptor, releasing the active intracellular domain of NICD which goes to the nucleus and interacts with transcription factors CSL to activate transcription of Notch-responsive genes and luciferase (Fig. 5k). After transfection (12-16 hours), Media was changed, and HEK293 cells were cultured in the presence or absence of FBLN2. After 24 hours of cultivation, luciferase activity was measured using Dual-Luciferase Assay System (BPS Bioscience) and luminometer. The ratio of Firefly luminescence to Renilla luminescence was used to normalize luciferase activity.

Statistics analysis

Microsoft Excel (V 2201 Build 16.0.14827.20198) was used for collating data. All graphs were generated using GraphPad Prism 9.4.0 (LaJolla). For comparisons between two groups, significance was determined by unpaired two-tailed Student's t-tests for parametric data and Mann-Whitney test for non-parametric data. Where multiple groups were compared, one/two-way ANOVA with Bonferroni or Tukey's multiple comparison test and non-parametric Kruskal Wallis with Dunn's multiple comparison test were used. EAE disease scores were analyzed with two-way repeated-measures ANOVA with Dunnett's multiple comparisons test. Kolmogorov-Smirnov test was applied to verify normal distribution of data. p values below 0.05 was considered statistically significant shown by asterisks in the figures (*$p < 0.05$, **$p < 0.01$,***$p < 0.001$).

Reporting summary

Further information on research design is available in the Nature Research Reporting Summary linked to this paper.

Data availability

The scRNA-seq and bulk RNA-seq data will be deposited in the NCBI Sequence Read Archive: *to be completed prior to publication*. All datasets generated in this study are available from the corresponding author on reasonable request.

There are no restrictions on data availability. Source data are provided with this paper.

Methods references

1. Kumar, N. et al. The Development of an AAV-Based CRISPR SaCas9 Genome Editing System That Can Be Delivered to Neurons. Front Mol Neurosci 11, 413 (2018). https://doi.org:10.3389/fnmol.2018.00413

2. Doench, J. G. et al. Optimized sgRNA design to maximize activity and minimize off-target effects of CRISPR-Cas9. Nat Biotechnol 34, 184-191 (2016). https://doi.org:10.1038/nbt.3437

3. Sanson, K. R. et al. Optimized libraries for CRISPR-Cas9 genetic screens with multiple modalities. Nat Commun 9, 5416 (2018). https://doi.org:10.1038/s41467-018-07901-8

4. Platt, R. J. et al. CRISPR-Cas9 knockin mice for genome editing and cancer modeling. Cell 159, 440-455 (2014). https://doi.org:10.1016/j.cell.2014.09.014

5. Challis, R. C. et al. Publisher Correction: Systemic AAV vectors for widespread and targeted gene delivery in rodents. Nat Protoc 14, 2597 (2019). https://doi.org:10.1038/s41596-019-0155-5

6. Chan, Ken Y et al. Engineered AAVs for efficient noninvasive gene delivery to the central and peripheral nervous systems. Nature neuroscience vol. 20,8 (2017). https://doi.org/10.1038/nn.4593

7. Weaver, A. et al. An elevated matrix metalloproteinase (MMP) in an animal model of multiple sclerosis is protective by affecting Th1/Th2 polarization. FASEB J 19, 1668-1670 (2005). https://doi.org:10.1096/fj.04-2030fje

8. Lozinski, B. M. et al. Exercise rapidly alters proteomes in mice following spinal cord demyelination. Sci Rep 11, 7239 (2021). https://doi.org:10.1038/s41598-021-86593-5

9. Zhang, R. et al. Enhanced liver X receptor signalling reduces brain injury and promotes tissue regeneration following experimental intracerebral haemorrhage: roles of microglia/macrophages. Stroke Vasc Neurol (2023). https://doi.org:10.1136/svn-2023-002331

10. Butler, A., Hoffman, P., Smibert, P., Papalexi, E. & Satija, R. Integrating single-cell transcriptomic data across different conditions, technologies, and species. Nat Biotechnol 36, 411-420 (2018). https://doi.org:10.1038/nbt.4096

11. Ghorbani, S. et al. Versican promotes T helper 17 cytotoxic inflammation and impedes oligodendrocyte precursor cell remyelination. Nat Commun 13,1 2445 (2022). https://doi:10.1038/s41467-022-30032-0

12. Dong, Y. et al. Oxidized phosphatidylcholines found in multiple sclerosis lesions mediate neurodegeneration and are neutralized by microglia. Nat Neurosci 24, 489-503 (2021). https://doi.org:10.1038/s41593-021-00801-z

Acknowledgements

We thank the Hotchkiss Brain Institute Advanced Microscopy Platform Facility, Molecular Core Facility, Hena Ramay and the Centre for Health Genomics and Informatics Bioinformatics Core, and Snyder Institute's Live Cell Imaging Resource laboratory at the University of Calgary, for their help. We thank the UK Multiple Sclerosis and Parkinson's Tissue Bank at Imperial College, London, for the MS brain tissues. We thank Dr. Walter Hader for his provision of human adult specimens for tissue culture. We would like to recognize the guidance that we received from Dr. Mariano Valpiano (SUNY, New York). We gratefully acknowledge Dr. Erin L. Stephenson (University of Calgary) for her neuropathology expertise. We thank Dr. Hedwich Kuipers (University of Calgary) for reagent sharing. This work was funded by operating grants from Department of Defense (DOD) grant, Multiple Sclerosis Canada (MSC) and Canadian Institutes of Health Research (CIHR) to V.W.Y. (W81XWH2210468, 3527 and FDN 167270, respectively). We also acknowledge operating grant support for the stroke analyses to M.X. from the National Key Research and Development Program of China (grant no: 2018YFC1312200), and the National Natural Science Foundation of China (grants no:

82071331 and 81870942). S.G. acknowledges postdoctoral fellowship support from Harley N. Hotchkiss Postdoctoral Fellowship, MSC and CIHR. C.L. received studentship fundings from the HBI Graduate Recruitment Scholarship and CIHR. B.M.L. and D.M. acknowledge studentships from the Alberta Graduate Excellence Scholarship, Harley N. Hotchkiss Doctoral Scholarship in Neuroscience and MSC. Y.D. received postdoctoral fellowship support from CIHR and Alberta MS Collaboration. H.L. acknowledges China Scholarship Council funding for her PhD studies. V.W.Y. acknowledges salary support from Canada Research Chair (Tier 1).

Author contributions

S.G. designed the project and performed the majority of experiments, analyzed the results, and wrote the first draft of the paper. C.L. performed some of the staining, imaging and western blot experiments. B.M.L. performed lysolecithin surgeries. D.M. helped with coronal sectioning and tissue processing. C.D. was critical for performing the scRNA-seq experiments and processing bulk sequencing data. Y.D. provided support for neuron and microglia culture. F.V. generated AAV vectors. C.S. helped with AAV injections. H.L.and M.X. contributed to the ICH data. V.W.Y. supervised the study, provided operational support, and edited and finalized the manuscript. All authors reviewed and edited the manuscript.

Competing interest declaration

The authors declare no competing interests.

Supplementary information

Supplementary Figure 1: Uncropped scans of source data for immunoblots. Shown are original Western blots with specific cropped bands used in Extended data figures in this study.

Supplementary Table 1. Positive differentially expressed genes from each cluster identified from scRNA-seq.

Supplementary Table 2. Differentially expressed genes (DEG) in oligodendrocyte lineage cells of FBLN2 deficient mice vs. WT.

Supplementary Table 3. Positive differentially expressed genes from each sub-cluster of oligodendrocyte lineage cells identified from scRNA-seq.

Figure 1

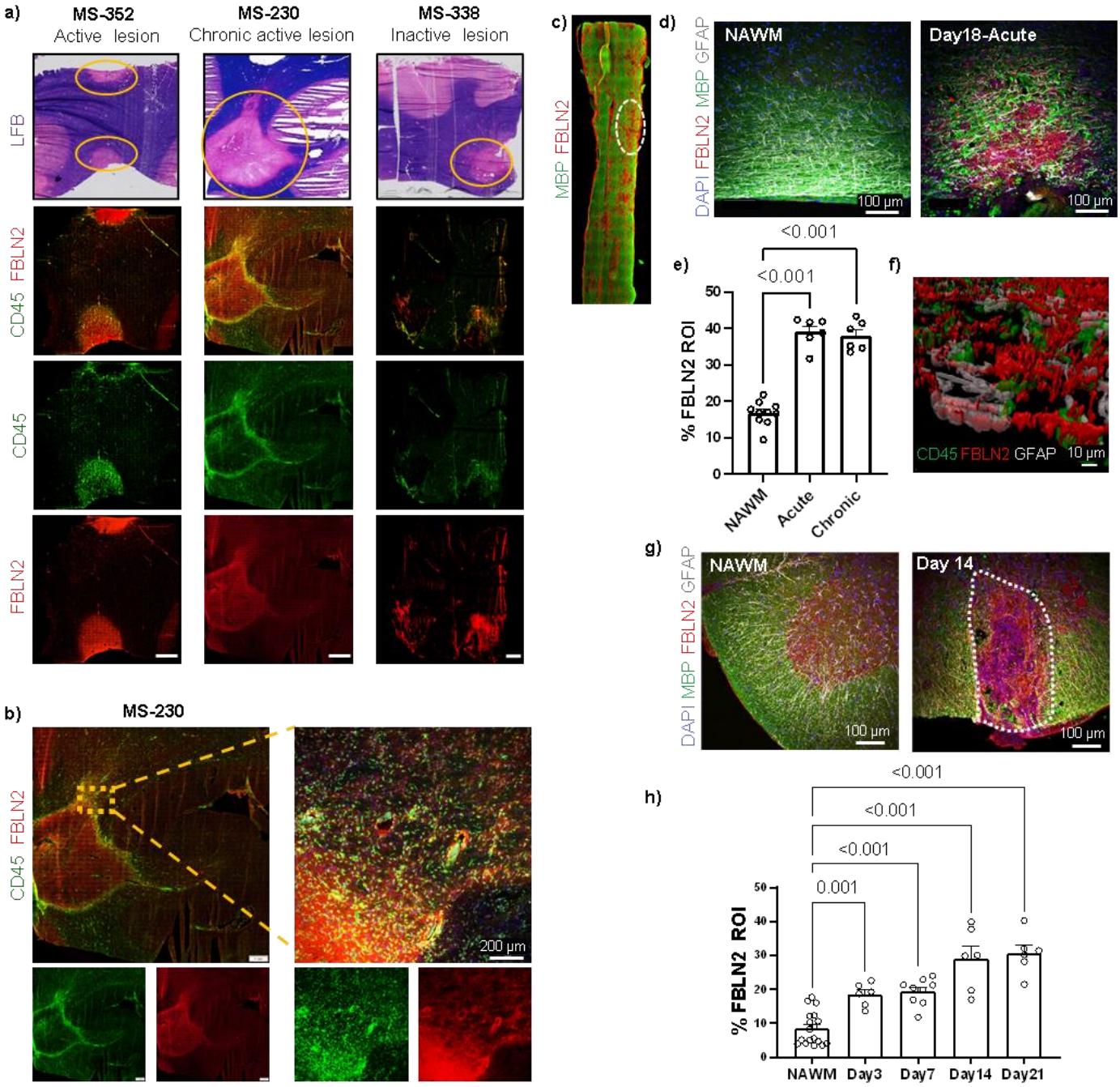

Figure 1. FBLN2 is upregulated in lesions of MS and its animal models.

a, Top: Luxol fast blue (LFB) and hematoxylin-eosin (H&E) histological-stained tissues showing demyelinated lesions from three MS brain samples (MS-230, 352, 338). White matter lesions were defined by loss of LFB staining. Yellow rings specify the lesion

areas. Bottom: Immunofluorescent images labeled with CD45 for immune cells and FBLN2. Scale bar, 2 mm. **b,** Yellow dotted square in the left panel of the image from MS-230 specify the area shown at higher magnification to the right. Scale bar, 200μm. **c,** Representative image of large area of longitudinal section of spinal cord from EAE mice. White dotted ring indicates an ROI tracked by loss of myelin. **d,** Representative images of spinal cord sections from EAE mice comparing the normal appearing white matter (NAWM) and lesion area. Scale bar, 100 μm. **e,** Quantification comparing the percent of FBLN2 in NAWM and EAE lesions at different time points. $n = 6$ mice total per group. Data were acquired from 2 separate experiments and each dot represents mean of 5 lesions analyzed per mouse. **f,** Colocalization of FBLN2 in $GFAP^+$ astrocytes but rarely $CD45^+$ immune cells using Imaris and 3D rendering. FBLN2 is also in acellular areas likely depicting deposition in the ECM. Scale bar, 10 μm. **g,** Representative images of coronal sections of NAWM and lysolecithin-induced demyelination lesion 14 days post injury. Dotted line indicates the lesion areas. Scale bar, 100 μm. **h,** Bar graph comparing the percent of FBLN2 area within the lysolecithin lesion over the time post injury. n=6 mice for day 3, 14 and 21, n=9 mice for day 7 from two separate experiments. Images in **a** and **c** were obtained by slide scanner. Images in **b, d, f** and **g** were acquired by immunofluorescent laser confocal microscope (Z-stack). Data in **e** and **h** are presented as Mean ± SEM; One-way ANOVA - Bonferroni post hoc.

Figure 2

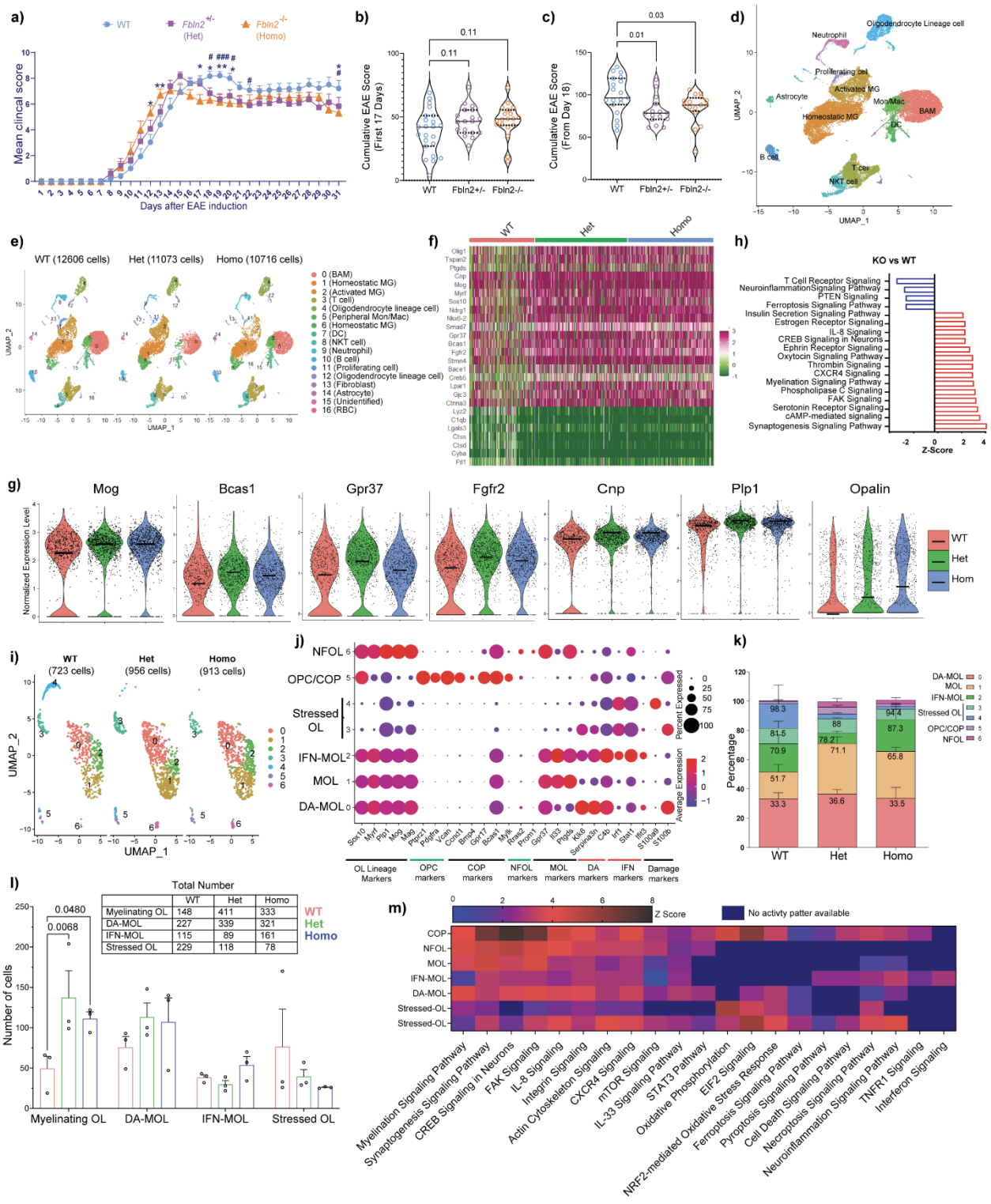

	WT	Het	Homo
Myelinating OL	148	411	333
DA-MOL	227	339	321
IFN-MOL	115	89	161
Stressed OL	229	118	78

Figure 2. The better clinical recovery from EAE in FBLN2 deficient mice is associated with an increase in myelinating oligodendrocyte density.

a, Average EAE clinical score (Mean ± SEM) is shown (*n*= 23 mice for WT, 18 mice for *Fbln2+/-,* 19 mice for *Fbln2-/-* from 3 independent experiments. Two-way repeated-measures ANOVA (Mixed-effects Model), Dunnett's multiple comparisons test;*p <0.05, **p < 0.01; # WT vs. *Fbln2+/-* , * WT vs. *Fbln2-/-*). **b,c,** Violin plots comparing the cumulative EAE scores for the first 17 Days (b) and from Day 18 post induction (c)**.** Medians are shown by a black horizontal line and dashed lines indicate the interquartile range **(**Kruskal-Wallis test, followed by Dunn's multiple comparison tests). **d,e,** UMAP plot of 34,395 cells from spinal cords of 9 EAE mice (d) and across different experimental groups (e) depicting 17 clusters as determined by 30 principal components and 0.3 clustering resolution. **f,g,** Heatmap (f) and Violin plots (g) comparing the levels of select DEGs associated with remyelination in oligodendrocyte cluster. Midline in the plot is the median. **h,** Select top activated (red) or inactivated (blue) pathways in oligodendrocyte from Het and Homo FBLN2 KO spinal cords compared to WT spinal cords as predicted by IPA. **i,** UMAP plots of 2592 oligodendrocyte lineage cells re-clustered into 7 distinct cell populations (principal components:10; clustering resolution: 0.4). **j,** Dot plot of representative marker genes enriched in oligodendrocyte. The size of the dot corresponds to the percentage of cells expressing the gene in each cluster. The color represents the average gene expression level. **k,l,** Bar graphs depicting percentage (k) and number (l) of cells in different subclusters of oligodendrocytes across groups (two-way repeated-measures ANOVA with Sidak's post-hoc test). **m,** Heatmap showing the Z-scores of predicted pathways by

IPA in oligodendrocyte subcluster. High Z scores depict predicted activation and low Z scores represent predicted inhibition of respective pathways. ScRNA-seq data in each experimental group acquired from 3 mice.

Figure 3

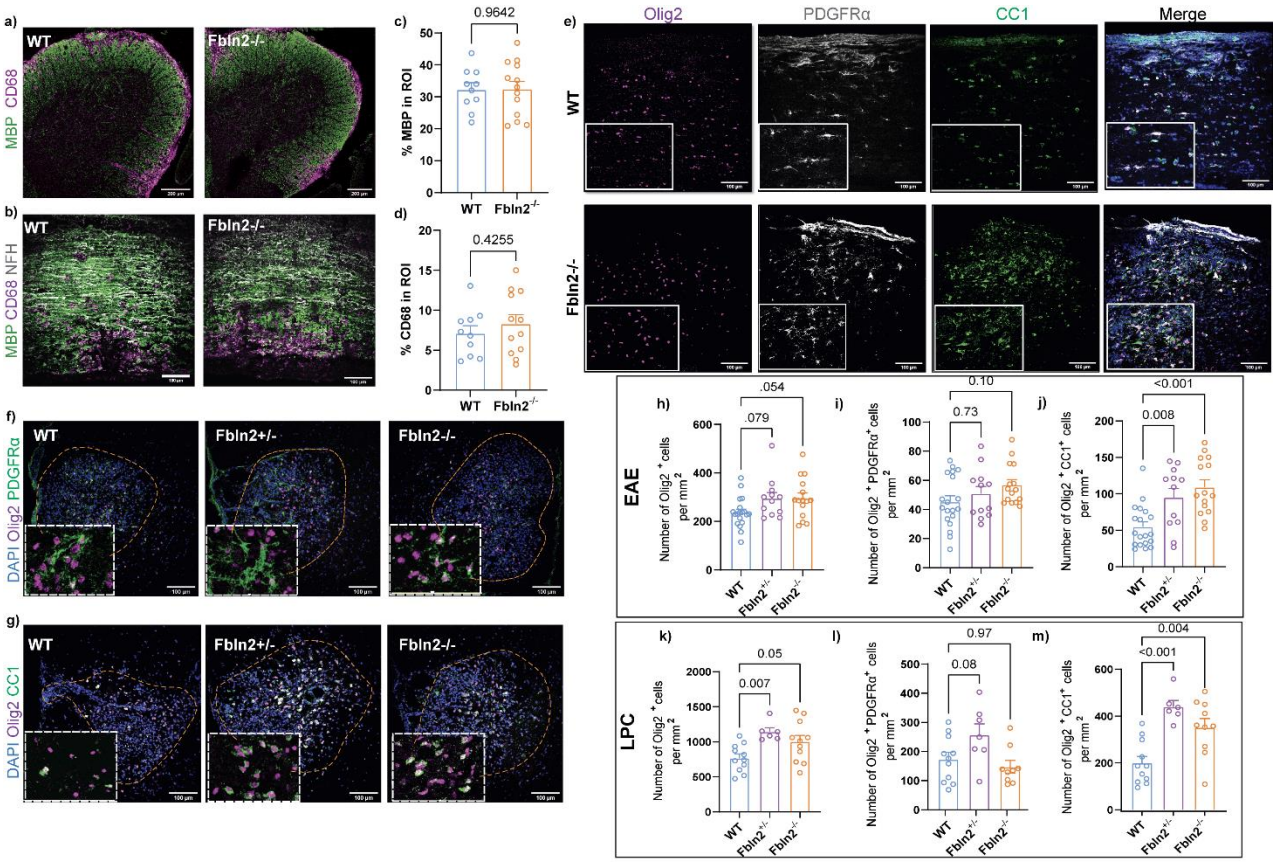

Figure 3. FBLN2 deficiency increases number of mature oligodendrocytes in demyelinating lesions.

a,b, Representative images of coronal (a) and longitudinal (b) sections of spinal cord from EAE mice comparing WT and *Fbln2-/-* mice. Tissues were stained for MBP and CD68. **c,d,** Bar graphs comparing the percent of ROI that is MBP^+ (c) or $CD68^+$ (d) (*n* = 10-12 mice; two-tailed unpaired Student's t test). **e-g,** Representative images of longitudinal sections of spinal cord from EAE mice (e) and coronal sections of lysolecithin lesions 14 dpi (f, g) stained for DAPI, Olig2, PDGFRα and CC1. **h-m,** Bar graphs comparing the number of $Olig2^+$ Lineage cells, $Olig2^+$ $PDGFR\alpha^+$ OPCs and $Olig2^+$ $CC1^+$ mature oligodendrocytes per mm^2 within EAE (h-j) and lysolecithin (k-m)

lesions. *n* = 19 mice for WT, 12 mice for *Fbln2+/-* and 15 mice for *Fbln2-/-* over 3 separate EAE experiments; *n* = 11 mice for WT, 7 mice for *Fbln2+/-* and 10 mice for *Fbln2-/-* over 2 separate lysolecithin experiments; One-way ANOVA - Bonferroni post hoc. Data are presented as Mean ± SEM. All images were acquired by immunofluorescent laser confocal microscope (Z-stack). Scale bars, 100 μm.

Figure 4

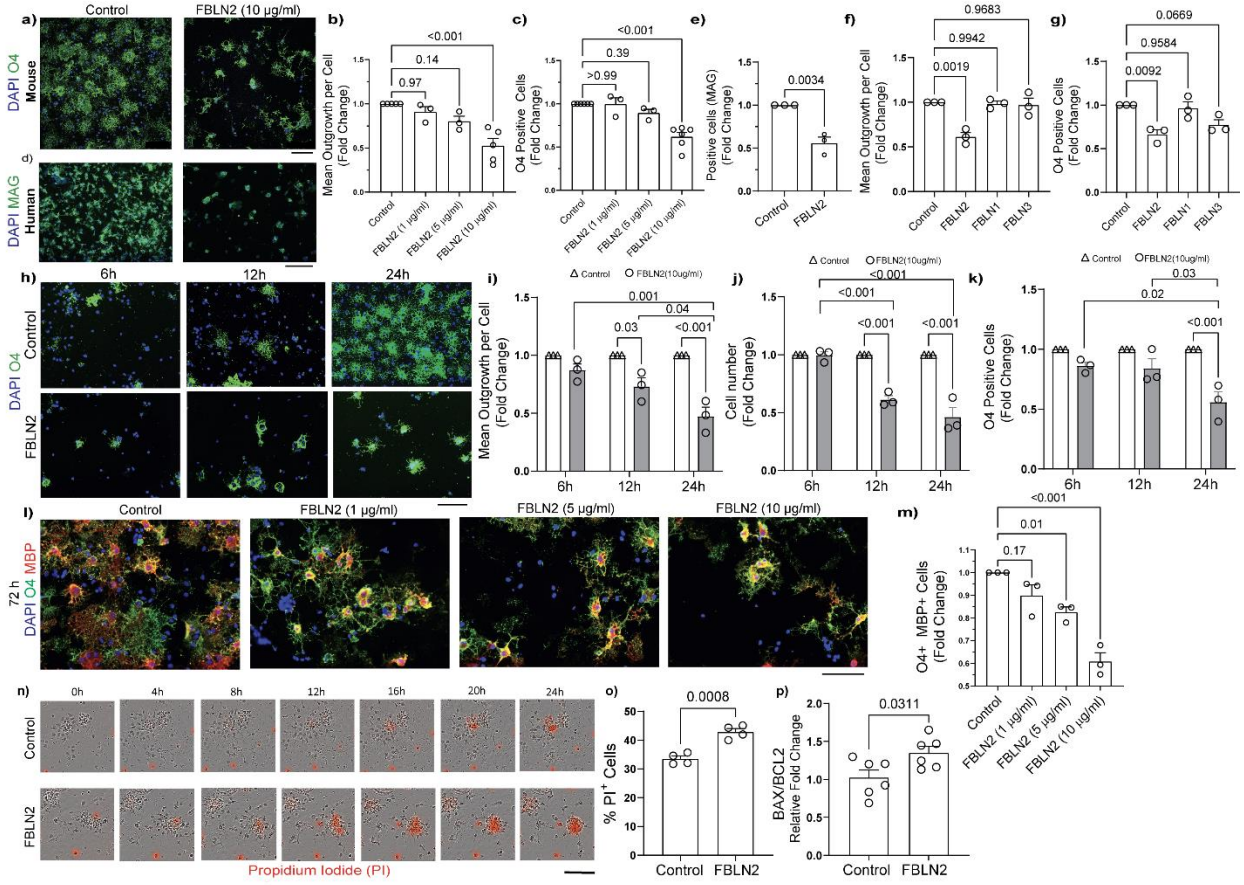

Figure 4. FBLN2 impairs maturation of oligodendrocytes and induces cell death. **a,** Representative images of mouse OPCs stained for the sulfatide O4 24 h after plating onto PBS (control) and FBLN2 coated wells. **b,c,** Bar graphs showing the fold change in mean process outgrowth (b) and number of $O4^+$ cells (c) of mouse OPCs cultured on control and coated wells with different concentrations of FBLN2 for 24 h (*n*= 5 independent experiments for FBLN2 (10 µg/ml), *n*=3 for FBLN2 (1 and 5 µg/ml); One-way ANOVA - Bonferroni post hoc). **d,** Representative images and **e,** bar graph showing number of MAG^+ cells from human OPCs cultured on control and FBLN2 (10 µg/ml) coated wells (*n*= 3 independent experiments; two-tailed unpaired Student's t test). **f,g,** Quantification of mean process outgrowth (f) and number of $O4^+$ cells (g) of mouse

OPCs cultured on coated wells with different members of FBLN family (10 µg/ml) (*n*= 3 independent experiments; One-way ANOVA - Bonferroni post hoc). **h-k,** Representative images of mouse OPCs (h) and bar graphs comparing the fold change in mean process outgrowth (i), number of total cells (j) and number of $O4^+$ cells (k) at different time points (6,12 and 24 h) after plating onto control and FBLN2 (10 µg/ml) coated wells (*n*= 3 independent experiments; Two-way ANOVA - Bonferroni post hoc). **l,** Representative images of mature mouse oligodendrocytes stained for O4 (green) and MBP (red) 72 h after plating on control and coated wells with different concentration of FBLN2. **m,** Quantification comparing the number of $O4^+$ MBP^+ cells (*n*= 3 independent experiments; One-way ANOVA - Bonferroni post hoc). **n,** Representative images from live imaging of mouse OPC plated on control and FBLN2 (10 µg/ml) coated wells in the presence of propidium iodide (PI) at different time points. **o,** Bar graph showing the proportion of PI^+ OPCs after 24h (*n*= 3 independent experiments; two-tailed unpaired Student's t test). Each experiment (dot) included 3–4 replicates. Scale bar,100 µm. **f,** Ratio of Bax to Bcl-2 mRNA expression in mouse OPCs using Real time PCR (*n*= 6 replicates over two separate experiments, two-tailed unpaired Student's t test). Data are presented as Mean ± SEM.

Figure 5

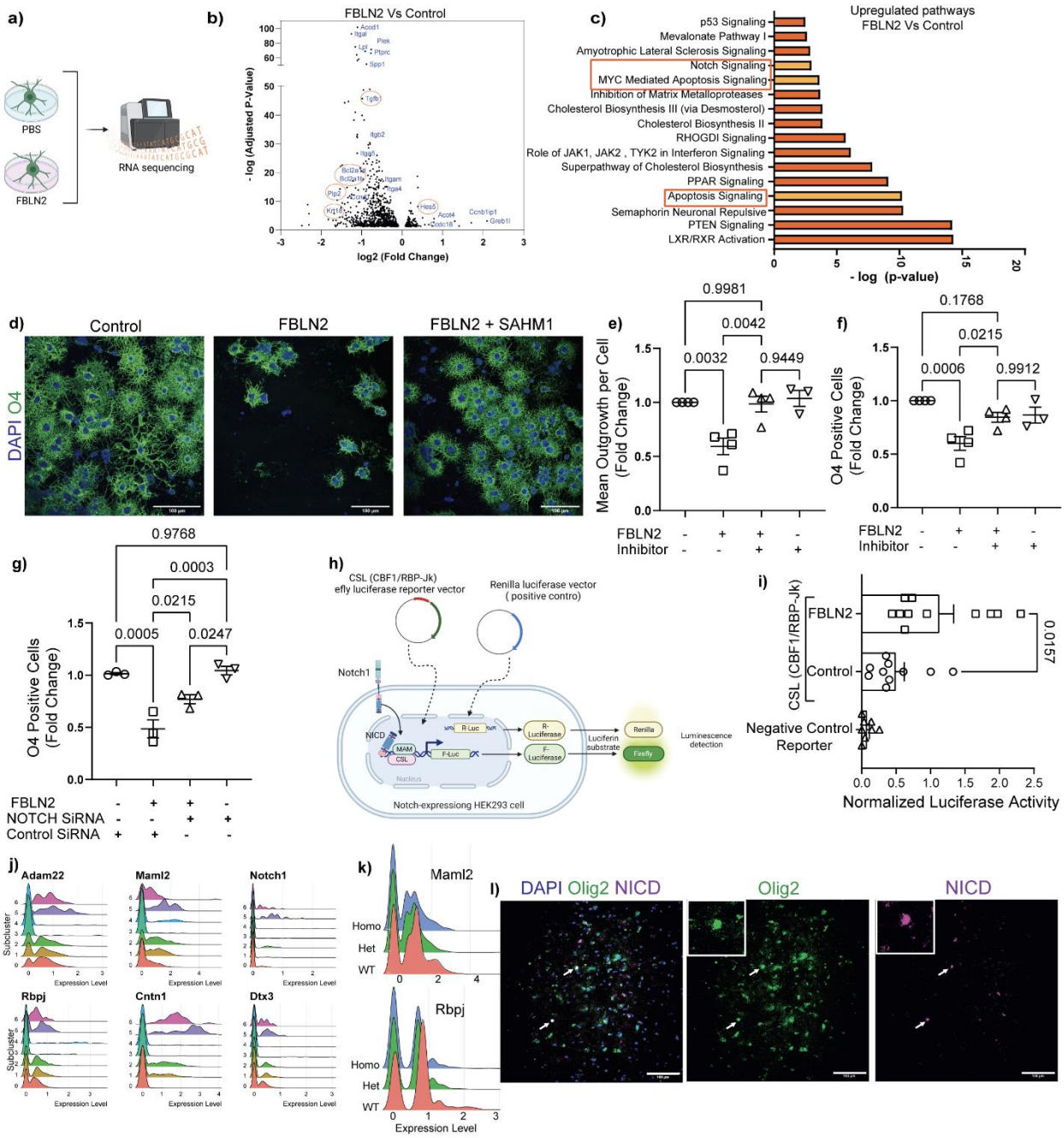

Figure 5. Blocking Notch pathway rescues the inhibitory effect of FBLN2 on oligodendrogenesis.

a, Schematic diagram of the experimental design. Created with BioRender.com **b,** Volcano plots showing differentially upregulated or downregulated genes in mouse

OPCs cultured on FBLN2 (10 µg/ml) coated wells for 6h, identified by RNA sequencing. **c,** Top up-regulated pathways predicted by IPA from DEGs by mouse OPCs in the presence of FBLN2. RNA sequencing data were acquired from 3 replicates per group (PBS or FBLN2). **d-g,** Representative images (d) and quantification for mean process outgrowth (e) and number of $O4^+$ cells (f) of mouse OPCs cultured on control and FBLN2 (10 µg/ml) coated wells with or without Notch inhibitor (SAHM1, 10µM) after 24h (*n*= 4 independent experiments); or transfected with two NOTCH1 siRNA (g, 200nM/each, *n*= 3 independent experiments; One-way ANOVA - Tukey post hoc). Scale bar,100 µm. **h,** Schematic depicting the Notch pathway reporter assay using the constitutively expressing Renilla luciferase vector (positive control) and CSL (CBF1/RBP-Jk) Firefly luciferase reporter vector. **i,** Bar graph comparing the relative luciferase activity (Firefly to Renilla) in Hek239 cells transfected with luciferase reporter or negative control vectors in the presence or absence of 10 µg/ml FBLN2 (*n*= 8-10 replicates over two separate experiments; One-way ANOVA - Bonferroni post hoc). Each experiment in e, h-j included 3–4 replicates. Data are presented as Mean ± SEM. **j,k,** Ridge plots comparing expression of select genes involved in Notch pathway across oligodendrocyte subclusters (0: DA-MOL, 1: MOL, 2: IFN-MOL, 3 and 4: Stresses-OL, 5: COP, 6: NFOL) (j) and experimental groups (k). **l,** Immunofluorescent images of MS brain sample labeled with Olig2 and NICD for activated Notch. White arrows show the presence of Notch signaling in oligodendrocytes. Scale bar, 100 µm.

Figure 6

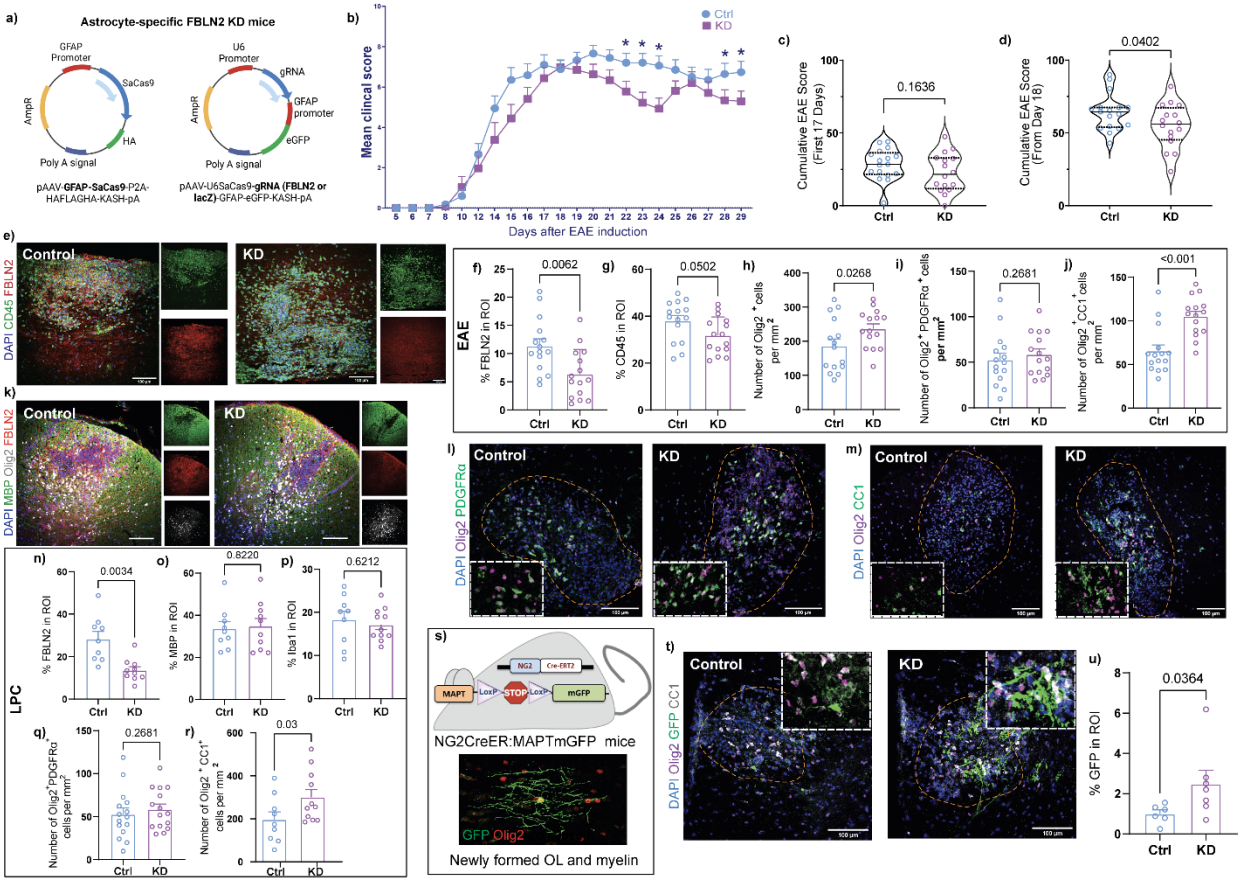

Figure 6. **Astrocytic deletion of FBLN2 improves functional recovery in EAE which is associated with more robust oligodendrogenesis.**

a, Schematic showing the genome of AAVs used in this study. AAVs were injected retro-orbitally at 3 × 10^{11} vg/virus per mouse 2 weeks before EAE induction or lysolecithin surgery for targeted disruption of FBLN2 (KD) or non-target guide RNA (Ctrl). **b,** Average EAE clinical score (Mean ± SEM). **c,d,** Violin plots comparing the cumulative EAE scores for the first 17 days (c) and from Day 18 (d). Black lines represent medians and quartiles are shown by dashed lines. (*n*= 17 mice for Ctrl, 15 mice for KD from 3 independent experiments, Mann-Whitney test; *$p < 0.05$). **e-g,** Representative images of longitudinal spinal cord sections from EAE mice (g) and

quantifications for FBLN2 (h) and CD45 (i) percent area of the lesion. **h-j)** Graphs comparing number of Olig2$^+$ OL lineage cells (h), Olig2$^+$ PDGFRα$^+$ OPCs (i) and Olig2$^+$ CC1$^+$ mature oligodendrocytes (j) per mm^2 of EAE lesions (*n*= 15 mice per group over 3 separate experiments). **k-r,** Representative images of lysolecithin lesions 14 dpi (k-m) and quantifications comparing percent area of FBLN2, MBP, Iba1 (n-p) and number of OPCs (q) or mature oligodendrocytes (r) per mm^2 of lesion ROI (*n*= 9 mice for Ctrl, 11 mice for KD over 3 separate experiments). **s,** NG2^{CreER}:MAPT^{mGFP} mice were used to identify newly formed oligodendrocytes and myelin as GFP$^+$. **t,** Representative images of lysolecithin lesions 14 dpi from NG2^{CreER}:MAPT^{mGFP} mice that had received AAVs 2 weeks before lysolecithin-surgery. **u,** Bar graph showing the extent of GFP in lesions (*n*= 6 mice over 2 separate experiments). Data in f-j, n-r and u are presented as Mean ± SEM; two-tailed unpaired Student's t test). Images were acquired by immunofluorescent laser confocal microscope (Z-stack). Scale bar, 100 µm.

Extended Data Figure 1

a)

Up- and Down-regulated ECM proteins in spinal cord of EAE mice

Gene nam	Description	fold change	pvalue	Category
Nid1	Nidogen-1	38.34	0.005	ECM Glycoproteins
Lama4	Laminin subunit alpha-4	23.46	0.006	ECM Glycoproteins
Prelp	Proline arginine-rich end leucine-rich repeat	9.62	0.047	Proteoglycans
Fbln2	**Fibulin-2**	**9.47**	**0.011**	**ECM Glycoproteins**
Bgn	Biglycan	9	0.043	Proteoglycans
Col24a1	Collagen alpha-1(XXIV) chain	6.89	0.04	Collagens
Col4a2	Collagen alpha-2(IV) chain	6.29	0.021	Collagens
Nid2	Nidogen-2	5.1	0.021	ECM Glycoproteins
Sbspon	Somatomedin-B and thrombospondin type-1 domain-containing protein	4.38	0.008	ECM Glycoproteins
Col12a1	Collagen alpha-1(XII) chain	3.48	0.042	Collagens
Lama2	Laminin subunit alpha-2	3.45	0.003	ECM Glycoproteins
Fgg	Putative uncharacterized protein	3.15	0	ECM Glycoproteins
Lamc3	Laminin subunit gamma-3	2.95	0.005	ECM Glycoproteins
Postn	Periostin	2.92	0.004	ECM Glycoproteins
Aebp1	Adipocyte enhancer-binding protein 1	2.9	0.049	ECM Glycoproteins
Hspg2	Basement membrane-specific heparan sulfate proteoglycan core protein	2.61	0.014	Proteoglycans
Emilin1	Putative uncharacterized protein	2.6	0.007	ECM Glycoproteins
Fn1	Putative uncharacterized protein	2.34	0.008	ECM Glycoproteins
Vwa5a	von Willebrand factor A domain-containing protein 5A	2.33	0	ECM Glycoproteins
Dcn	Decorin	2.27	0.033	Proteoglycans
Col5a3	Collagen type V alpha 3 chain	2.13	0.001	Collagens
Col14a1	Collagen alpha-1(XIV) chain	2.09	0.01	Collagens
Tgfbi	Transforming growth factor-beta-induced protein ig-h3	2.02	0.006	ECM Glycoproteins
Lamb1	Laminin B1 subunit 1	2	0.002	ECM Glycoproteins
Fga	Protein Fga	1.99	0	ECM Glycoproteins
Fbn1	Mutant fibrillin-1	1.95	0.024	ECM Glycoproteins
Spp1	Osteopontin	1.9	0.04	ECM Glycoproteins
Col18a1	Collagen alpha-1(XVIII) chain	1.9	0.003	Collagens
Lamc1	Laminin subunit gamma-1	1.8	0.003	ECM Glycoproteins
Vtn	Vitronectin	1.73	0.034	ECM Glycoproteins
Lamb2	Laminin subunit beta-2 GN=Lamb2	1.7	0.021	ECM Glycoproteins
Lama1	Laminin subunit alpha-1	1.69	0.006	ECM Glycoproteins
Fgb	Fibrinogen, B beta polypeptide, isoform CRA_a	1.65	0	ECM Glycoproteins
Col15a1	Collagen alpha-1(XV) chain	1.65	0.002	Collagens
Col3a1	MKIAA4231 protein (Fragment)	1.63	0.02	Collagens
Lgi1	Leucine-rich glioma-inactivated protein 1	0.62	0.007	ECM Glycoproteins
Slit2	MKIAA4141 protein (Fragment)	0.58	0.028	ECM Glycoproteins
Bcan	Brevican core protein	0.56	0.002	Proteoglycans
Lgi2	LGI2B brain-derived splice form	0.55	0.002	ECM Glycoproteins
Lgi3	Putative uncharacterized protein	0.55	0.001	ECM Glycoproteins
Hapln4	Hyaluronan and proteoglycan link protein 4	0.51	0.001	Proteoglycans
Ntng1	Netrin-G1	0.48	0.01	ECM Glycoproteins

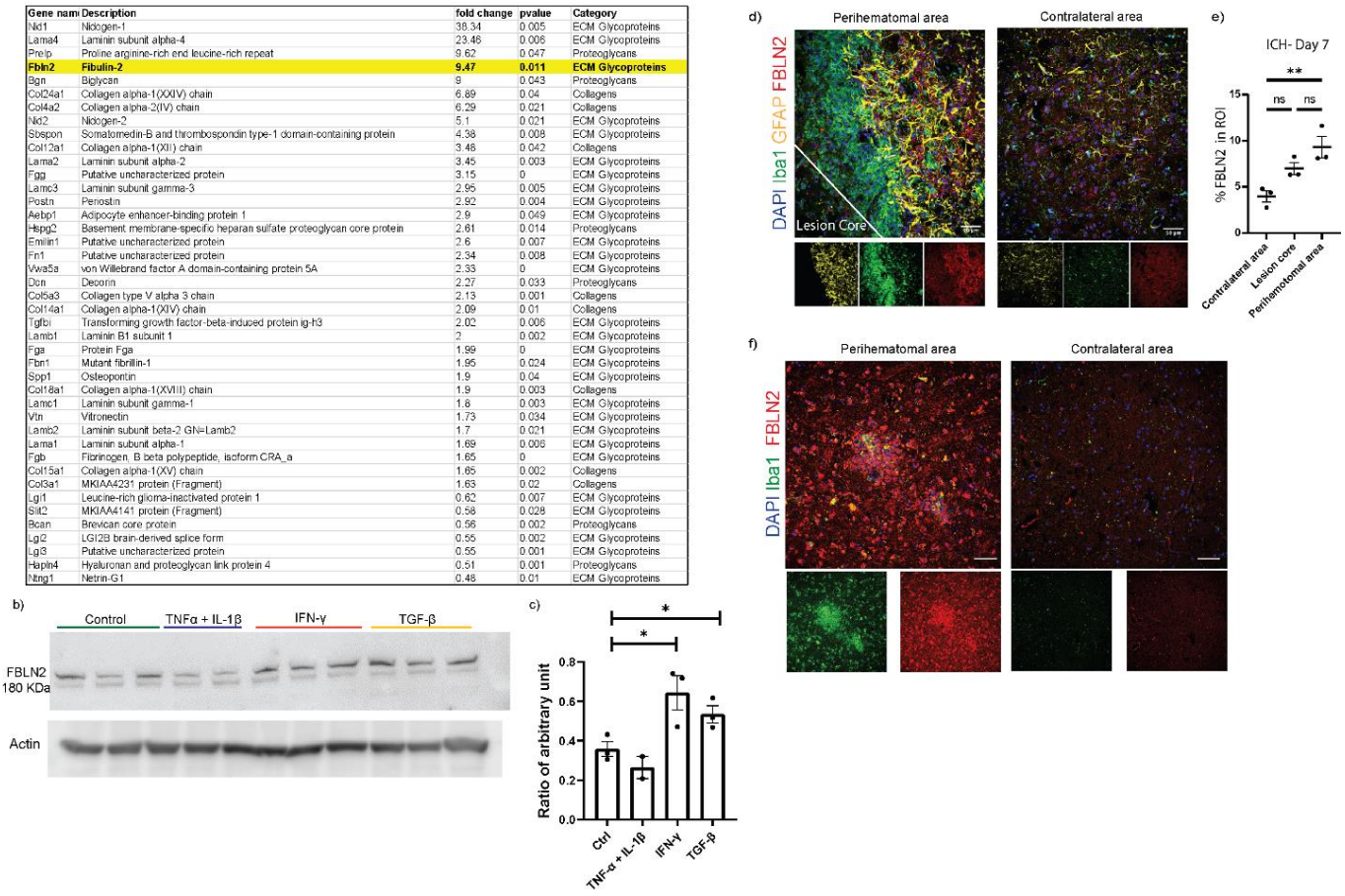

Extended Data Figure 1. FBLN2 is upregulated in activated astrocytes in culture and intracerebral hemorrhage (ICH) injury. **a,** Up- and down-regulated ECM proteins in spinal cord of EAE mice identified from a proteomic study[28]. **b,** Western blot analysis of FBLN2 in mouse astrocytes cultured with or without indicated treatments for 24 h. **c,** Bar graph comparing the signal ratio of FBLN2 to β-actin in untreated astrocyte (control) to TNF-α+IL1-β (10ng/mL each) , IFN-γ (10ng/mL) and TGF-β (10ng/mL) treated cells. *n*= 3 for control, IFN-γ and TGF-β groups, 2 for TNF-α+IL1-β group. **d,** Representative confocal images and **e,** FBLN2 percent area of perihematomal and contralateral (uninjured) region of the mouse brain 7 days after collagenase induced ICH (*n*= 3 mice).

f, Representative confocal images of human brain 3 days after hemorrhagic stroke comparing perihaematomal and contralateral (no evidence of pathology) areas. Data are presented as Mean ± SEM from one representative experiment. Experiments were repeated twice; One-way ANOVA - Bonferroni post hoc; *$p < 0.05$, **$p < 0.001$). Scale bar, 50 μm.

Extended Data Figure 2

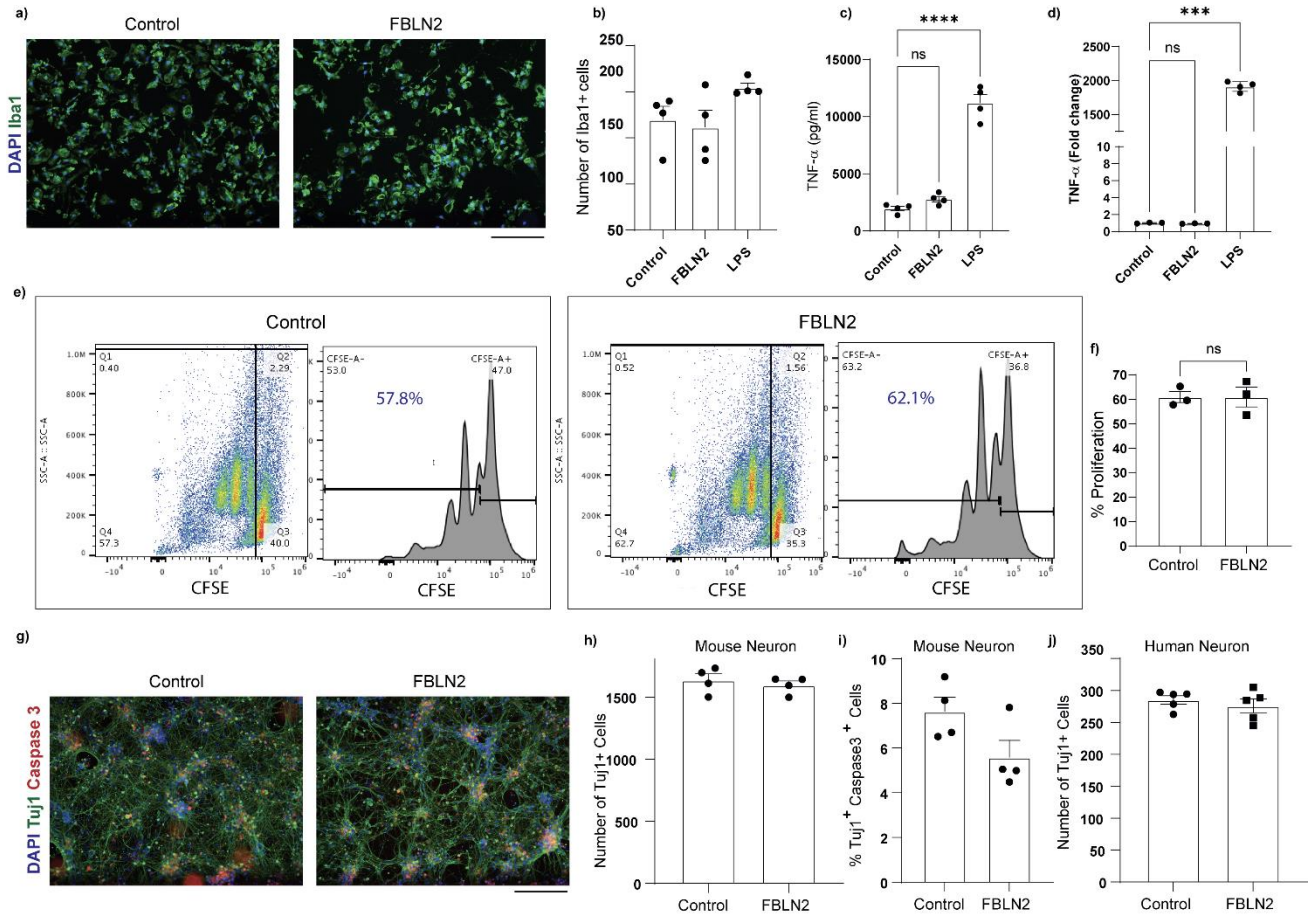

Extended Data Figure 2. FBLN2 does not affect microglia/macrophages, lymphocytes and neurons.

a, Representative images of primary mouse microglia labeled with Iba1 after 24h of culture on PBS (control) or FBLN2 (10 µg/ml) coated wells. **b,** Quantification comparing number of $DAPI^{+}Iba1^{+}$ microglia in the presence and absence of FBLN2 after 24h. **c,d,** Level of TNF-α measured by ELISA in the conditioned medium of mouse microglia (c) and bone marrow derived macrophages (d) treated with FBLN2 or LPS for 24h (*n* = 4 replicates; One-way ANOVA - Bonferroni post hoc; ***p < 0.001). **e,** FACS CFSE plots showing T cell proliferation after 3 days in the presence or absence of FBLN2 (10 µg/ml) where the peaks to the left represent cycles of cell division. **f,** Quantification comparing the percentage of dividing cells (*n* = 3

replicates, Two-tailed unpaired Student's t test). **g,** Representative images of primary mouse neurons labeled with β-tubulin (Tuj1) and caspase3 after 24 h of culture on PBS (control) or FBLN2 coated (10 µg/ml) wells. DAPI was used to label nuclei. **h-j,** Bar graph comparing the number of DAPI+Tuj1+ (h), percentage of Tuj1+ Caspase3+ (i) primary mouse neurons and number of DAPI+Tuj1+ primary human neurons (j) after 24 h (n = 4-5 replicates; two-tailed unpaired Student's t test). Data are presented as Mean ± SEM from one representative experiment. Experiments were repeated twice. Scale bar, 100 µm.

Extended Data Figure 3

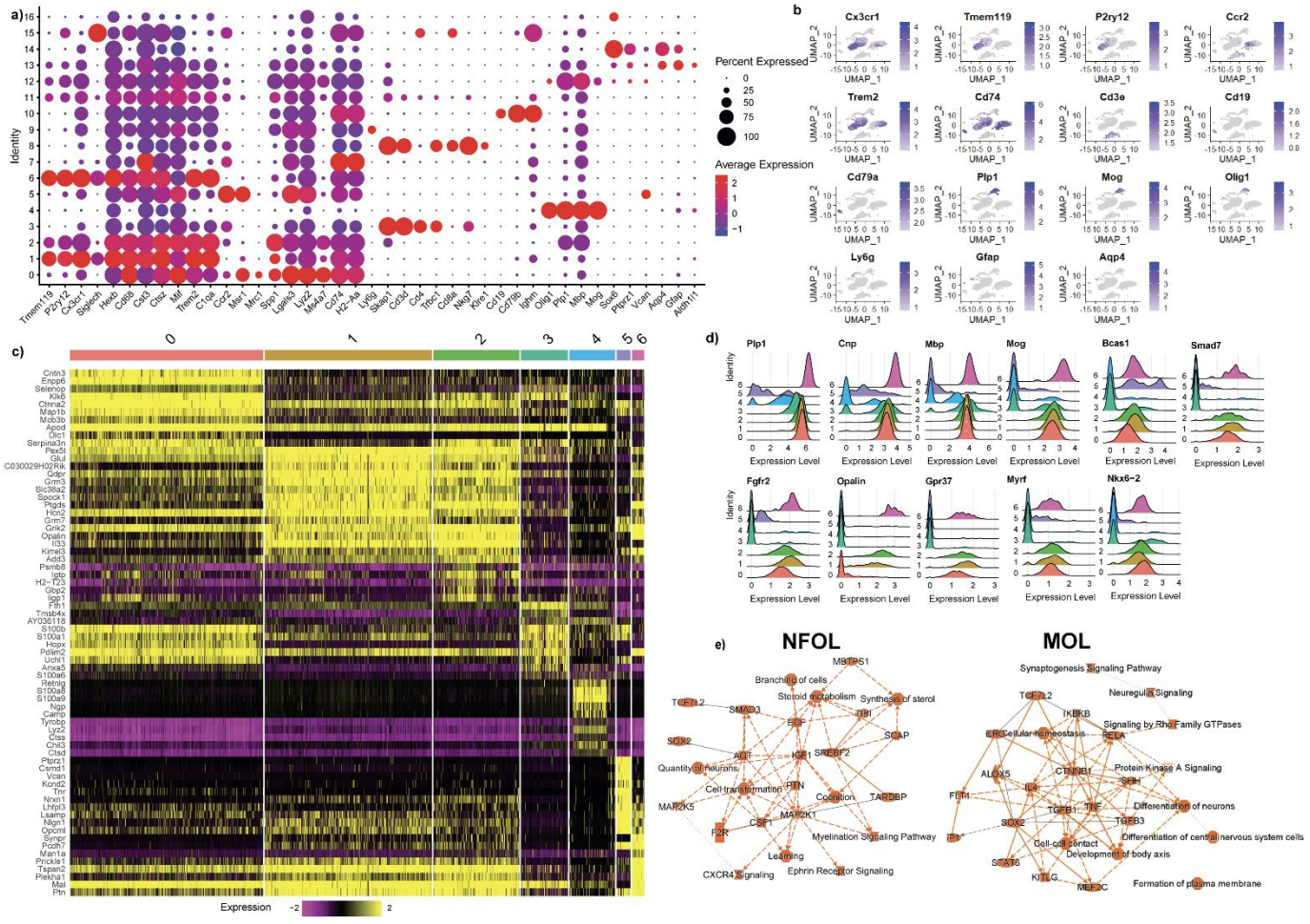

Extended Data Figure 3. Additional scRNA-seq analysis.

a, Dotplot showing the expression of lineage markers for homeostatic microglia, activated microglia or macrophages, BAM, DC, neutrophils, T cells, NKT cells, B cells, oligodendrocyte lineage cells and astrocytes across the clusters. The size of the dot corresponds to the percentage of cells expressing the gene in each cluster. The color represents the average gene expression level. **b,** Feature UMAP plot showing the distribution of various genes used to define clusters. Color bars indicate average expression. **c,** Heat map of top marker genes of different subclusters of oligodendrocyte

lineage cells. **d,** Ridge plots comparing expression of select remyelination-related genes across oligodendrocyte subclusters (0: DA-MOL, 1: MOL, 2: IFN-MOL, 3 and 4: Stresses-OL, 5: OPC/COP, 6: NFOL) **e,** Graphical summary of IPA predicted activated pathways in NFOL (subcluster 6) and MOL (subcluster 1). ScRNA-seq data in each experimental group acquired from 3 mice.

Extended Data Figure 4

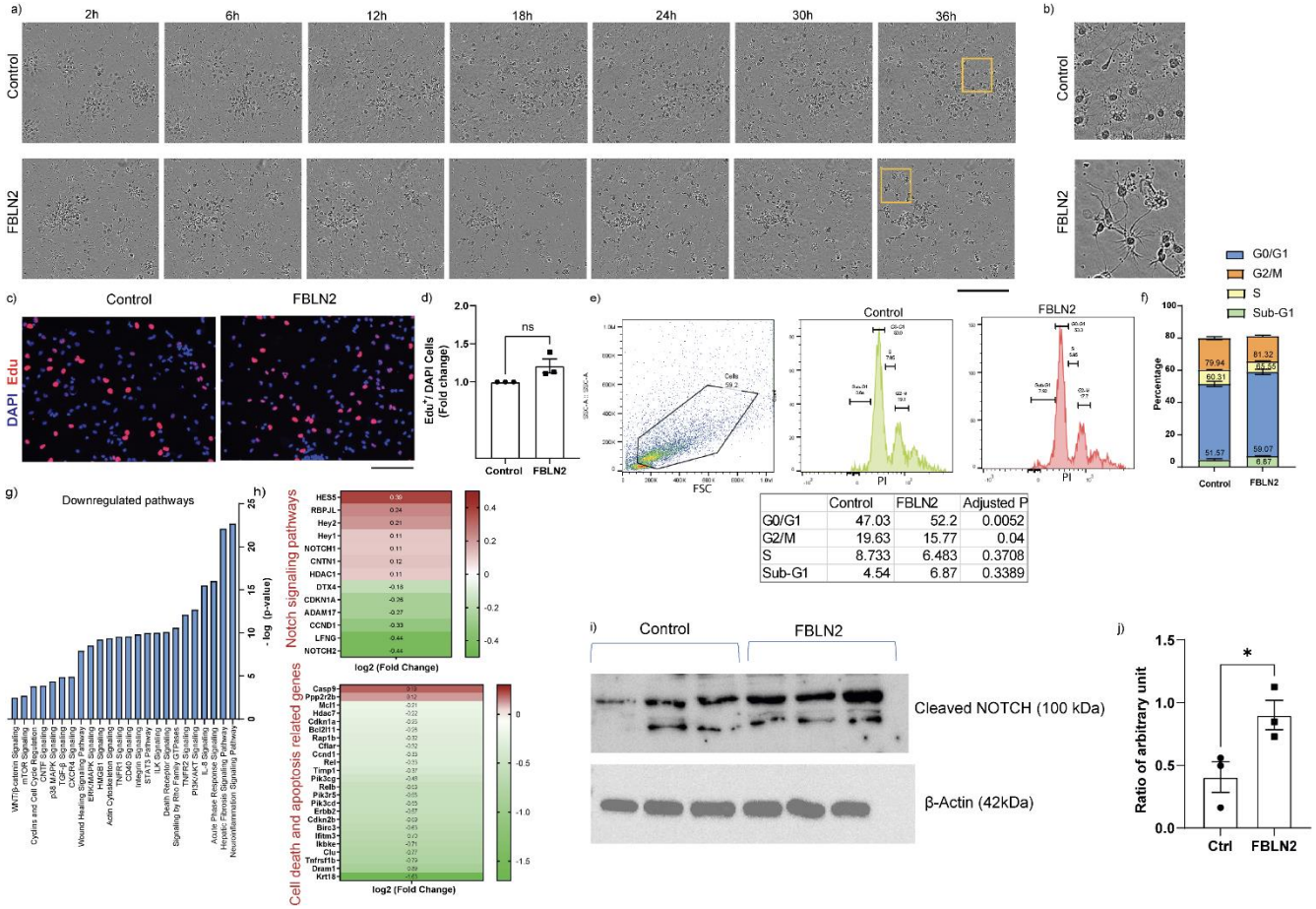

	Control	FBLN2	Adjusted P
G0/G1	47.03	52.2	0.0052
G2/M	19.63	15.77	0.04
S	8.733	6.483	0.3708
Sub-G1	4.54	6.87	0.3389

Extended Data Figure 4. FBLN2 does not inhibit OPC proliferation while it induces cell cycle arrest in differentiating OPCs.

a,b, Representative bright-field microscopy images from live imaging of mouse OPC plated on PBS (control) and FBLN2 (10 µg/ml) coated wells at different time points. Yellow boxes specify the areas shown at higher magnification in b. **c,d,** Representative images (c) and bar graph (d) comparing the proliferation of mouse OPCs in the presence or absence of FBLN2 (10 µg/ml) by measuring incorporation of EdU into DNA following 24h culture in the proliferation media (*n*= 3 replicates; two-tailed unpaired Student's t test). **e,** Cell cycle analysis using PI staining and flow cytometry of mouse OPCs cultured on control and FBLN2 (10 µg/ml) coated wells in

differentiation media after 12h. **f,** Bar graph and table depicting percentage of cells in different phases of cell cycle including sub-G1, G0/G1, S and G2/M phase (*n*= 3 replicates, two-way repeated-measures ANOVA with Sidak's post-hoc test). **g,** Top down-regulated pathways predicted by IPA from DEGs by mouse OPCs in the presence of FBLN2. **h,** Log2 (Fold Change) of genes associated with Notch signalling pathway (top), and cell death and apoptosis (bottom) by FBLN2 treated OPCs. RNA sequencing data were acquired from 3 replicates per group (control or FBLN2 (10 µg/ml)). **i,j,** Western blot analysis of cleaved NOTCH (NICD) (i) and quantification (j) comparing the signal ratio of NICD to β-actin in OPCs plated on control and FBLN2 (10 µg/ml) coated wells in differentiation media for 12 h (*n*= 3 replicates; Two-tailed unpaired Student's t test; *$p < 0.05$). Data are presented as Mean ± SEM from one representative experiment. Experiment was repeated twice. Scale bar,100 µm.

Extended Data Figure 5

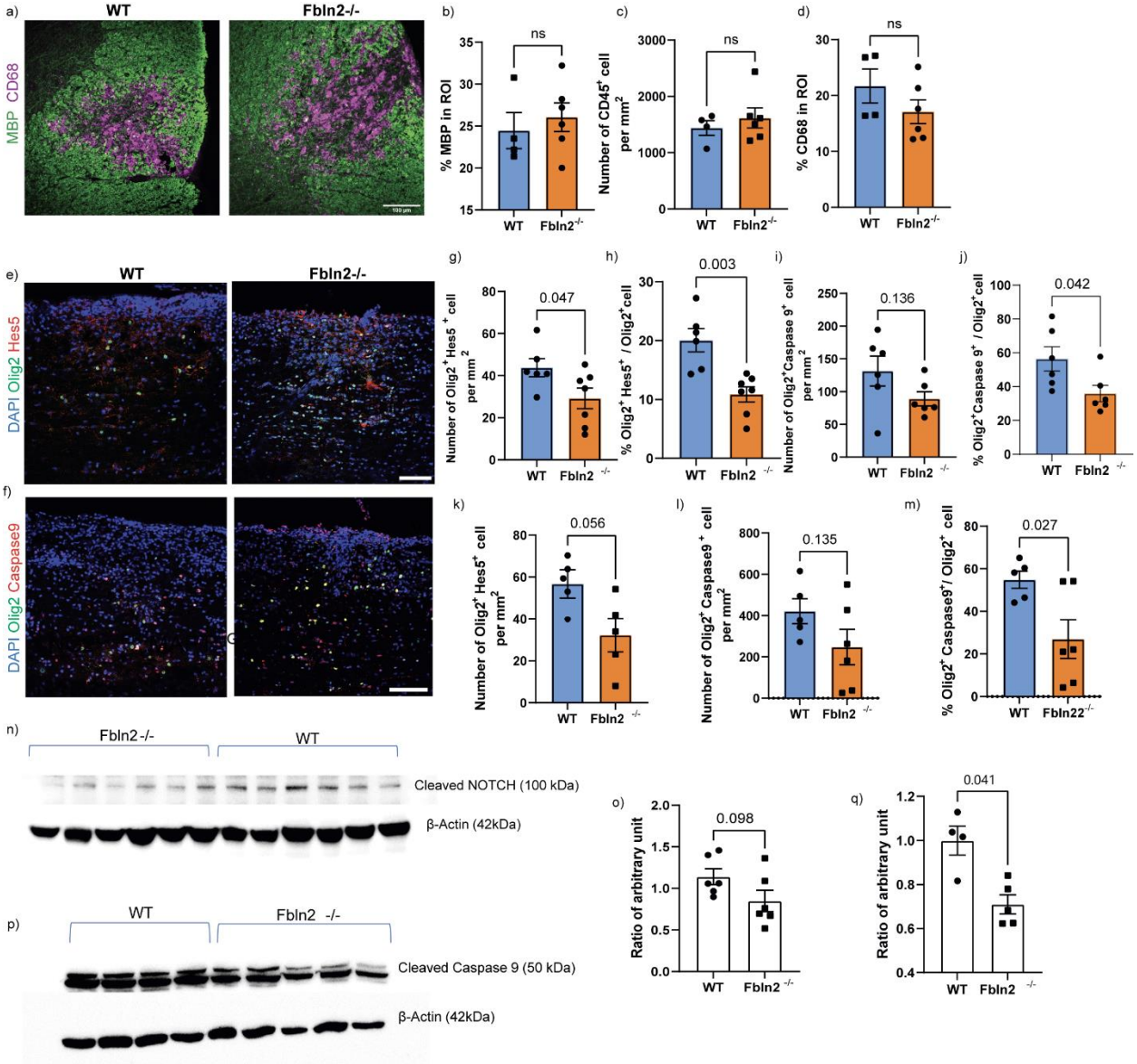

Extended Data Figure 5. Additional data from FBLN2 knockout mice.

a, Representative images of coronal sections of the lysolecithin lesions 14 dpi comparing wildtype (WT) and homozygous FBLN2 knockout mice (*Fbln2-/-).* Tissues were labeled with MBP and CD68. **b-d,** Bar graphs comparing the percent area of MBP (b), number of $CD45^+$ immune cells (c) and percent of the lesion ROI that is $CD68^+$ (d) ($n = 4$-6 mice). **e,f,** Representative images of longitudinal sections of spinal cord from EAE mice comparing WT and *Fbln2 -/-* mice. Tissues were stained for DAPI, Olig2 and Hes5 or cleaved caspase 9. **g-m,** Bar

graphs comparing the number (g) and proportion (h) of Olig2$^+$ Hes5$^+$ oligodendrocytes, number (i) and proportion (j) of Olig2$^+$ Caspase 9$^+$ oligodendrocytes within the EAE lesions (*n*= 6 mice); and number of Olig2$^+$ Hes5$^+$ oligodendrocytes (k), Olig2$^+$ Caspase 9$^+$ oligodendrocytes (l) per mm^2 and proportion of Olig2$^+$ Caspase 9$^+$ cells (m) within the ROI of lysolecithin lesions 14 dpi (*n*= 5-6 mice). **n,** Western blot analysis of cleaved NOTCH (NICD) and **o,** bar graph comparing the signal ratio of NICD to β-actin between WT and *Fbln2-/-* mice (*n*= 6 mice). **p,** Western blot analysis of cleaved caspase 9 and **q,** quantification for signal ratio of cleaved caspase 9 to β-actin in WT and *Fbln2-/-* mice (*n*= 4-5 mice). Data are presented as Mean ± SEM; two-tailed unpaired Student's t test. Images were acquired by immunofluorescent laser confocal microscope (Z-stack). Scale bars, 100 μm.

Extended Data Figure 6

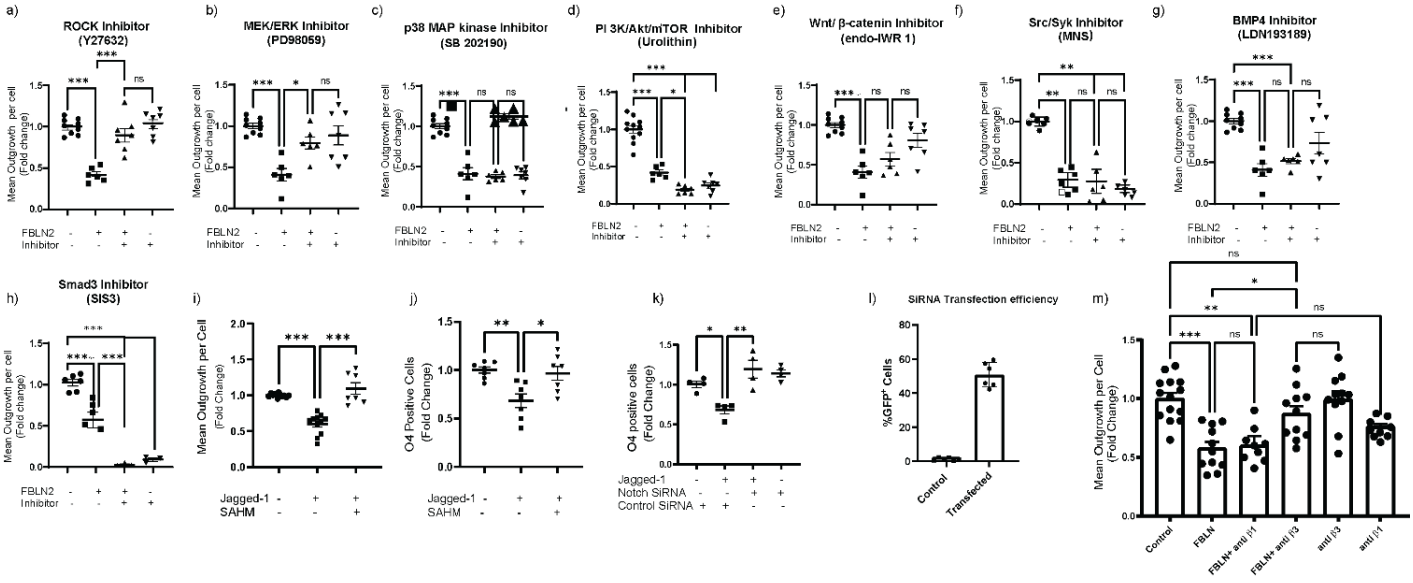

Extended Data Figure 6. Additional OPC culture experiments.

a-h, Bar graphs comparing the mean process outgrowth of mouse OPCs cultured on PBS (control) and FBLN2 (10 µg/ml) coated wells with or without 1µM ROCK (a), 10µM MEK/ERK (b), 10µM P38 MAP kinase (c), 10µM PI3k/AKT/mTOR (d), 1µM Wnt/βcatenin (e), 10µM Src/Syk (f), 100nM BMP4 (g) and 10µM Smad3 (h) signaling inhibitors after 24h (*n*= 6-9 replicates from 2-3 separate experiments). **i-j,** Quantification for mean process outgrowth (i) and number of $O4^+$ cells (j) of mouse OPCs cultured on control and Jagged1 (2µg/ml) coated wells with or without Notch inhibitor (SAHM1, 10µM) after 24h (*n*= 7 replicates over two separate experiments; each experiment included 3–4 replicates). **k,** Number of $O4^+$ cells of mouse OPCs transfected with two NOTCH1 siRNA (200nM) cultured on control and Jagged1 (2µg/ml) coated wells (*n*= 4 replicates from one representative experiment. Experiment was repeated twice). **l,** Percentage of GFP expressing cells showing the SiRNA transfection efficiency (~50%) (*n*= 6). **m,** Fold change in mean process outgrowth of mouse OPCs cultured on control and FBLN2 (10 µg/ml) coated wells with or without function blocking antibodies to the integrin β1or β3 (50

µg/ml) for 24h (*n*= 9-11 replicates over three separate experiments). Data are presented as Mean ± SEM, One-way ANOVA - Tukey post hoc; *$p < 0.05$, **$p < 0.01$, ***$p < 0.001$.

Extended Data Figure 7

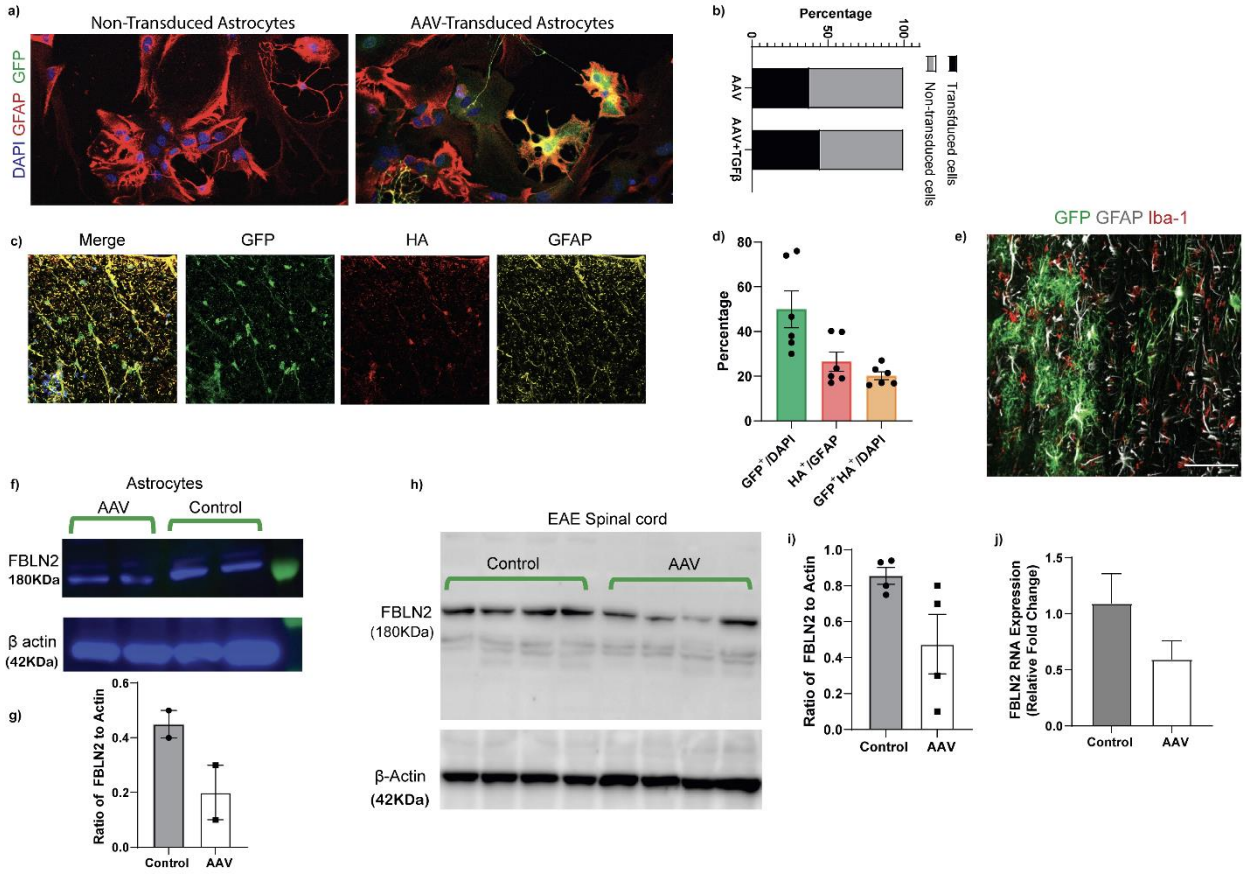

Extended Data Figure 7. Feasibility and success of AAV-coupled CRISPR/Cas9 system to target FBLN2 in astrocytes.

a, Representative images of mouse astrocytes stained for GFAP and GFP 48 h after transduction with GFP expressing AAV (1.5×10^6 vg/virus per 10000 cells). **b,** Graph showing the percentage of GFP^+ cells in AAV transduced or non-transduced astrocytes with or without TGF-β (10ng/mL) treatment (*n*= 3 replicates). **c,** Representative images of coronal sections of spinal cord from 8-week-old naive C57BL/6J mice 14 days post AAV injection (3 × 1011 vg/virus). Tissue was labeled with GFP, HA and GFAP. **d,** Quantification showing the percentage of GFP^+ cells, HA^+ astrocytes and double positive cells for GFP and HA (*n*= 6 ROIs from three mice). **e,** Representative image of longitudinal section of spinal cord from EAE mice (NAWM) labeled with GFP, GFAP and Iba1. **f,** Western blot analysis of FBLN2 in mouse non-

transduced and AAV-transduced astrocytes for 48h. **g,** Bar graph comparing the signal ratio of FBLN2 to β-actin in mouse non-transduced and AAV-transduced astrocytes. **h-l,** Western blot analysis of FBLN2 (h) and quantification (i) comparing the signal ratio of FBLN2 to β-actin in spinal cord lysate of AAV-injected EAE mice (FBLN2-targeted or non-target gRNA as control). **j,** Relative fold change of FBLN2 mRNA expression using Real time PCR in spinal cords of AAV-injected EAE mice (*n*= 4 mice). Data are presented as Mean ± SEM; two-tailed unpaired Student's t test for i and j, no significant difference.

Extended Data Figure 8

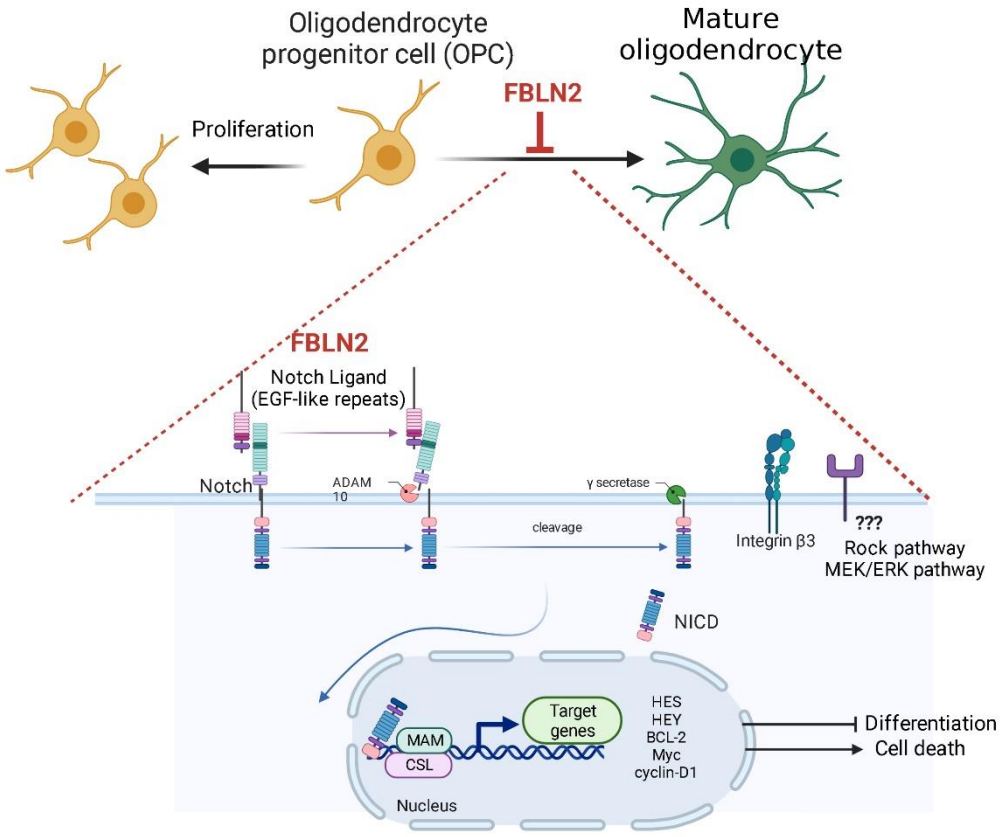

Extended Data Figure 8. FBLN2 engages Notch signaling pathway in differentiating-OPCs which impairs their maturation to oligodendrocytes in part through inducing cell death. Created by BioRender.